Journal of Materials Chemistry A

REVIEW

View Article Online
View Journal | View Issue

Cite this: J. Mater. Chem. A, 2019, 7, 9368

A review of nanostructured non-titania photocatalysts and hole scavenging agents for CO_2 photoreduction processes

Jeannie Z. Y. Tan * and M. Mercedes Maroto-Valer

Received 29th October 2018
Accepted 18th December 2018

DOI: 10.1039/c8ta10410g

rsc.li/materials-a

The imperative for the development of sustainable energy technologies to alleviate the heavy reliance on fossil fuels as well as to mitigate the serious environmental issues associated with CO_2 emission has fostered the development of solar fuels through CO_2 photoreduction. The well-documented TiO_2 and modified TiO_2-based photocatalysts have been shown to photoreduce CO_2 into hydrocarbons. Meanwhile, there is also an increasing interest in the utilisation of non-titania based materials, namely metal sulphides, oxides, oxynitrides and nitrides, for CO_2 photoreduction. Distinct from other published reviews, we discuss here recent progress made in designing metal sulphide, oxide, oxynitride and nitride photocatalysts for CO_2 photoreduction through morphological changes, aiming at providing a systematic summary of non-titania based materials for CO_2 photoreduction. Furthermore, the introduction of hole scavengers in order to maximise the CO_2 photoreduction efficiency is also reviewed.

1. Introduction

Fossil fuels are currently unrivalled for energy generation, and our existing infrastructure is built to handle fossil fuels for transportation, heating and electricity.[1] Our heavy reliance on fossil fuels results in annual emissions of 32 Gt of CO_2.[2] This is likely to increase to 36–43 Gt by 2035, subject to policies governing CO_2 emissions and energy use, even with increasing renewable energy sources.[3] To mitigate these environmental issues as well as alleviate our dependence on fossil fuels, harvesting the seemingly infinite solar energy and storing it in the form of chemical fuels hold significant promise to address current and future energy demands. Moreover, the chemical industry and a vast amount of chemical products rely heavily on using fossil fuel feedstock. This further motivates the development of sustainable processes to generate fuels and chemical feedstock from water and CO_2 using solar energy. Such a process is akin to photosynthesis in nature, and therefore, it is referred to as the artificial photosynthesis.

Photoelectrocatalytic reduction of CO_2 in aqueous suspensions using semiconducting powders was first proposed by Inoue *et al.* in 1979.[4] Later in 1987, the photocatalytic reduction of CO_2 to CH_4 in the presence of H_2O was proposed by Thampi *et al.*[5] Since then, an increasing number of studies on the photo(electro)catalytic reduction of CO_2 have been conducted (Fig. 1). Among these studies, almost 50% focused on the materials employed as photocatalysts for conversion of CO_2 under UV and/or visible irradiation. The rest of the studies concentrated mainly on modelling or process development. The use of TiO_2 as a photocatalyst for CO_2 reduction has been extensively studied and has been reviewed elsewhere.[6–10] However, the lack of systematic studies of non-TiO_2 semiconducting materials, namely metal sulphides, oxides, oxynitrides and nitrides, for CO_2 photoreduction (CO_2PR) has inhibited the development of these photocatalysts compared to titania-based photocatalysts.

Although different photocatalysts (*i.e.*, titania and non-titania based semiconductors) have been proposed in the literature, the overall CO_2PR conversion remains low especially under sunlight irradiation, making the CO_2PR system not practical for commercialisation. To further increase the efficiency of CO_2PR, the introduction of scavenging agents into the CO_2PR system has been proposed. However, so far, the introduction of hole scavenging agents has not been systematically studied, though studies started in the last century. Therefore, the necessity to systematically scrutinise the recent development of non-TiO_2 photocatalysts and hole scavenging agents for CO_2PR is of great demand.

There are enormous scientific and technical challenges involved in making even the simplest fuel, H_2, and even more so for carbon-based fuels by means of CO_2 photoreduction. Similar to other photocatalytic processes, solar-driven photocatalytic conversion of CO_2 in the presence of H_2O to hydrocarbon fuels uses semiconducting materials to harvest solar energy and provides active sites to allow the photocatalytic conversion process to occur. The basic steps of the photocatalytic process can be summarised as follows:

(1) generation of charge carriers (electron–hole pairs) by semiconducting materials upon absorption of photons with appropriate energy from the irradiation of light,

Research Centre for Carbon Solutions (RCCS), Heriot-Watt University, Edinburgh EH14 4AS, UK. E-mail: j.tan@hw.ac.uk

(2) separation of charge carriers and their transportation to the surface of the photocatalyst, and

(3) chemical redox reactions between the charge carriers and the reactants.

CO_2PR with H_2O into fuels is illustrated in Fig. 2. TiO_2 was the first material used for CO_2PR,[5] and since then it has been widely used because of its abundance, availability, high chemical stability, low cost and non-toxicity.[12] Despite the great effort made in the CO_2PR using TiO_2 and its derivative materials, the efficiency of the process remains low,[7] mainly attributed to the following factors:

(a) Rapid recombination of photogenerated electron–hole pairs;[10]

(b) Mild reducing power;

• The potential of the conduction band electrons is only slightly more negative than the multi-electron reduction potentials of CO_2, thus providing a very small driving force, whereas the potential of the valence band holes is much more positive than the water oxidation potential.[7]

(c) Limited visible light absorption due to the wide bandgap (3.0–3.2 eV) of TiO_2.[13,14]

Strategies including doping,[15,16] coupling with semiconductors,[17–19] dye sensitizing,[20,21] surface modification[22,23] *etc.* have been extensively used to improve TiO_2 photocatalysts and are summarised elsewhere.[9,14,24,25] However, the two most commonly used methods for extending the absorption range to visible light, namely sensitization or doping, do not fully address the optical issue of wide bandgap materials. Sensitizing agents (*e.g.*, dyes or quantum dots) often degrade when exposed to UV light and photogenerate oxidizing holes in TiO_2.[7] Dopant atoms, on the other hand, can become the centers of charge recombination. Moreover, the additional energy states associated with foreign atoms are highly localized, resulting in suppressed charge mobility.[27] Hence, while TiO_2 remains a benchmark photocatalyst, there is a lot of interest in developing other materials for CO_2PR, such as carbon-based semiconductors (*e.g.*, graphene-based composites,[28,29] carbon nanotube composites,[30] g-C_3N_4 based composites[31–33] and hybrid organic–inorganic materials[34–37]) and other inorganic transition or main group metal oxides, sulphides, oxynitrides, and nitrides. Since the use of carbon-based semiconductors for CO_2PR has been reviewed elsewhere,[30,34,38,39] these photocatalysts are not be discussed herein.

Inorganic semiconductors, namely metal oxides, sulphides, oxynitrides and nitrides, are among the first semiconductors

Dr Jeannie Z. Y. Tan received her BSc. (2010) from Universiti Sains Malaysia and her Msc. (2013) from Zhejiang University. She obtained her PhD (2017) from the University of Melbourne and after that joined the Research Centre for Carbon Solutions at Heriot-Watt University as a Research Associate. She is currently working on an EPSRC-funded project to develop innovative solutions for solar fuel conversion. She currently has 19 publications that have been cited over 200 times. She is also a reviewer for 2 journals (RSC Nanoscale Advances and Journal of Electronics & Telecommunication).

Prof M. Mercedes Maroto-Valer (FRSE, FIChemE, FRSC, and FRSA) is the Assistant Deputy Principal (Research & Innovation) and Director of the Research Centre for Carbon Solutions (RCCS) at Heriot-Watt University. She leads a multidisciplinary team of over 50 researchers developing novel solutions to meet the worldwide demand for energy. Her team's expertise comprises energy generation, conversion and industry, carbon capture, conversion, transport and storage, emission control, low carbon fuels, and low-carbon systems. She has over 450 publications, of which she edited 4 books, and 32% of her publications are among the top 10% most cited publications worldwide. Her research portfolio includes projects worth ~£35m, and she has been awarded a prestigious European Research Council (ERC) Advanced Award. She obtained a BSc with Honours (First Class) in Applied Chemistry in 1993 and then a PhD in 1997 at the University of Strathclyde (Scotland). Following a one-year postdoctoral fellowship at the Centre for Applied Energy Research (CAER) at the University of Kentucky in the US, she moved to Pennsylvania State University in the US, where she worked as a Research Fellow and from 2001 as an Assistant Professor and became the Program Coordinator for Sustainable Energy. She joined the University of Nottingham as a Reader in 2005, and within 3 years she was promoted to Professor in Energy Technologies. During her time at Nottingham she was the head of the Energy and Sustainability Research Division at the Faculty of Engineering. In 2012, she joined Heriot-Watt University as the first Robert Buchan Chair in Sustainable Energy Engineering and has served as the head of the Institute for Mechanical, Processing and Energy Engineering (School of Engineering and Physical Sciences) and the pan-University Energy Academy. She is a member of the Directorate of the Scottish Carbon Capture and Storage (SCCS). She holds leading positions in professional societies and editorial boards, and has received numerous international prizes and awards, including the 2018 Merit Award Society of Spanish Researchers in the United Kingdom (SRUK/CERU), 2013 Hong Kong University William Mong Distinguished Lecture, 2011 RSC Environment, Sustainability and Energy Division Early Career Award, 2009 Philip Leverhulme Prize, 2005 U.S. Department of Energy Award for Innovative Development, 1997 Ritchie Prize, 1996 Glenn Award—the Fuel Chemistry Division of the American Chemical Society and 1993 ICI Chemical & Polymers Group Andersonian Centenary Prize.

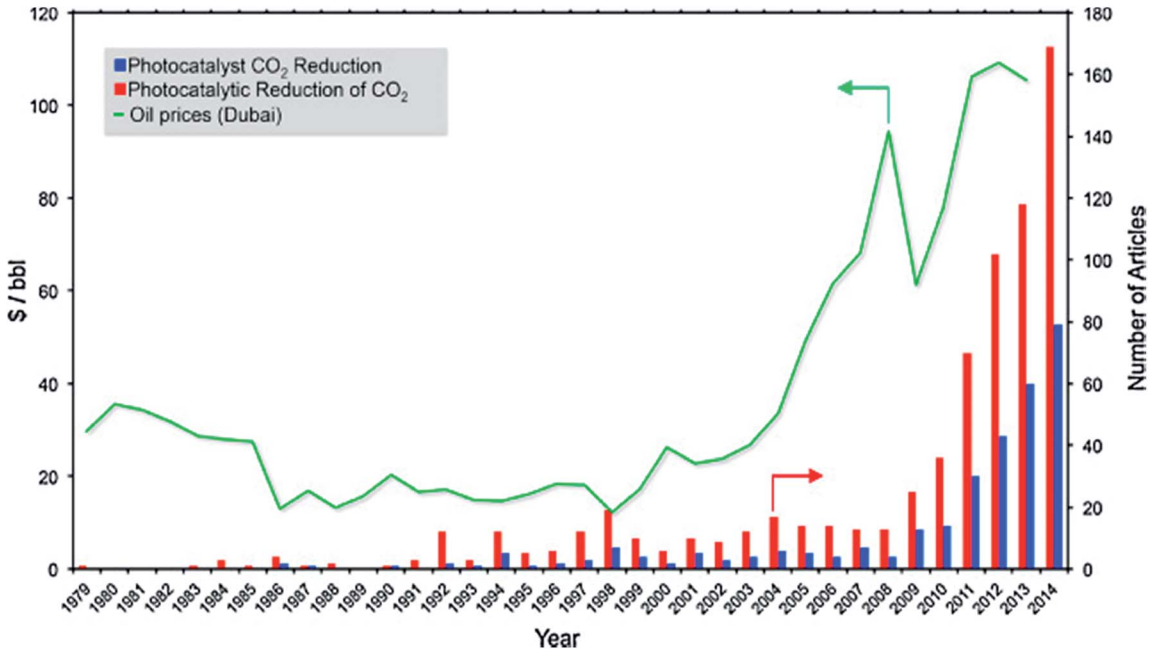

Fig. 1 Timeline for the number of articles published on CO_2 photoreduction *vs.* the price of oil. Reproduced from ref. 11 with permission.

used for solar-driven reactions. They possess relatively high stability, are low cost and absorb light consisting of photons with energy equal to or greater than their bandgap.[40] This very diverse group of materials includes both narrow and wide bandgap semiconductors; yet many of them offer a more favourable bandgap than TiO_2. Moreover, many recent CO_2PR developments follow similar trends to those for photocatalytic water splitting, as both processes share similar constraints on energy bands.[41–43] Specifically, the quest for new semiconductor materials is focused on the following points:[27]

(a) rising the valence band energy to decrease the bandgap,

(b) moving the conduction band to more reductive potentials,

(c) improving the quantum efficiency of exciton formation whilst suppressing charge recombination and

(d) using novel nanoscale morphologies to provide a large surface area with multiple photocatalytically active sites.

To achieve the quest mentioned above, different methods have been proposed previously and are reviewed in the following sections.

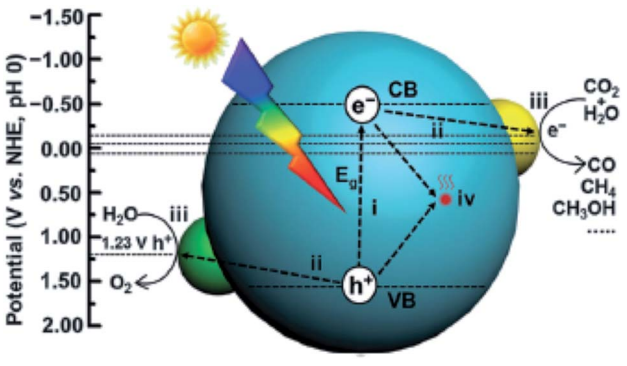

Fig. 2 Schematic illustration of photocatalytic CO_2 reduction with H_2O over a heterogeneous photocatalyst. The dotted lines indicate the thermodynamic potentials for water oxidation and CO_2 reduction into CO, CH_3OH and CH_4. Reproduced from ref. 26 with permission.

2. Non-TiO_2 materials for CO_2 photoreduction reactions

Although the position of conduction and valence bands is important for photocatalytic properties, the morphology of materials plays a critical role. Furthermore, manipulating the microstructure has also shown to alter the bandgap energy,[44] suppress the charge recombination,[45] enhance the diffusion of electrons towards the surface of photocatalysts,[46] induce quantum confinement effects[47] and provide more photocatalytic active sites, thereby enhancing the photocatalytic performance. In this section, nanostructured non-TiO_2 semiconducting materials for CO_2PR published in the last two decades are reviewed, including metal sulphides, oxides, oxynitrides and nitrides.

2.1 Sulphides

Sulphide semiconductors received a lot of attention for CO_2PR. This was because their valence band, made of 3p orbitals of the sulphur atoms, is located higher than those of their oxide analogues, resulting in the conduction band being more reductive.[42] Many sulphides have a narrow bandgap (*e.g.*, PbS and Bi_2S_3), with the absorption onset in the visible and infrared regions. Amongst sulphide semiconductors, ZnS and CdS were the most studied sulphides for CO_2PR. ZnS is a wide bandgap semiconductor ($E_g = 3.66$ eV in the bulk); however, it possesses

a strong reducing power of the conduction band ($E_{CB} = -1.85$ V *vs.* the NHE at pH 7).[48]

Zinc-based materials. The surface area of the photocatalyst is one of the key factors that can significantly affect the efficiency of the photocatalytic process. Kočí *et al.* proposed the immobilization of ZnS on montmorillonite, a representative natural clay mineral, which possesses a high surface area and layered structure, to optimise the efficiency of the CO_2PR (Table 1 entry 1).[49] The study demonstrated that the amount of ZnS loaded affected the degree of agglomeration that consequently influenced the electronic configuration as well as the efficiency of the ZnS/montmorillonite nanocomposite in the CO_2PR under UV irradiation (254 nm). A similar approach was demonstrated by Petra *et al.*, in which ZnS was loaded onto large-surface-area SiO_2 (340 $m^2\ g^{-1}$) to reduce CO_2 to formate using 2,5-dihydrofuran as the reducing agent.[50] The study revealed that the loading amount of ZnS significantly affected the yield and the optimal loading was 13% of ZnS into SiO_2, resulting in 7 mmol $g^{-1}\ h^{-1}$ of HCOOH. Nonetheless, the fabricated samples with coverages above 7% of ZnS on the SiO_2 matrix could suppress the photo-corrosion of ZnS to Zn(0), which is the major disadvantage of sulphides in an aqueous dispersion because the oxidation of lattice S^{2-} ions leads to elemental sulphur and eventually to sulphate.[51]

Meng *et al.* proposed the co-doping of Cd and Cu into ZnS as one of the most active and optimised design routes for metal sulphide photocatalysts so far.[52] It was found that the doping of Cu could promote the formation of S vacancies and narrow the bandgap energy of ZnS, whereas surface modification of Cu-doped ZnS with Cd^{2+} enhanced the product selectivity towards HCOOH (99%) under solar light irradiation. Recently, solid solutions of $ZnLn_2S_4$ with a flower-like microstructure decorated with a cubic CeO_2 co-catalyst have been shown to exhibit enhanced CH_3OH production (0.542 μmol $g_{catalyst}^{-1}\ h^{-1}$) when compared to pristine CeO_2 and $ZnLn_2S_4$ (0.139 and 0.073 μmol $g_{catalyst}^{-1}\ h^{-1}$, respectively) under visible light irradiation ($\lambda \geq$ 420 nm).[53]

Cadmium-based materials. CdS (2.4 eV and the absorption onset at 520 nm) is a narrow bandgap metal sulphide photocatalyst. Hence, CdS suffers from rapid recombination of photogenerated electron–hole pairs. In order to enhance the separation of photogenerated electron–hole pairs, surface-phase junctions deduced by the same semiconductors were proposed. Chai *et al.* fabricated a mixed-phase CdS that is composed of wurtzite and zinc-blende crystalline phases recently (Table 1 entry 2).[54] The fabricated sample exhibited a long photogenerated electron lifetime and efficient charge transfer. The maximum CO and CH_4 evolution rate was 1.61 and 0.31 μmol $h^{-1}\ g^{-1}$, respectively, and these production rates were maintained even after 100 h.

The conduction band of CdS is less reductive ($E_{CB} = -0.9$ V at pH 7 *vs.* NHE) than that of ZnS. Therefore, CdS is always decorated with noble metals, such as Ag. For instance, Zhu *et al.* proposed that the loaded Ag could act as an electron trap as well as an active site for CO_2PR on CdS.[55] The photoproduction of CO was improved by three times when compared with that obtained with bare CdS. Alternatively, CdS can be supported with other wide bandgap semiconductors to enhance its reducing power for CO_2PR. Kisch *et al.* found that the coupling of CdS with ZnS strongly enhanced the CO_2PR activity when compared to SiO_2-supported CdS or ZnS samples because CdS and ZnS can absorb light at ≤530 nm and ≤330 nm, respectively.[56] The study reported that 5 wt% CdS loaded onto ZnS induced a 40-fold and 16-fold enhancement in the production of HCOOH (~80 mM, $\lambda \geq$ 320 nm, 3 h) when compared to unmodified CdS and ZnS, respectively. This strong enhancement was attributed to the electronic semiconductor–support interaction effect that improved the charge separation efficiency of the coupled semiconductor system. A similar observation was also reported by Kočí *et al.* recently, in which core–shell CdS/ZnS nanoparticles deposited on montmorillonite prepared by a one-pot synthesis exhibited enhanced CO_2PR activity in water under UV irradiation ($\lambda = 365$ nm).[57] The increase in the yield was due to the enhanced charge separation of CdS cores by ZnS shells, the increase of surface area and the inhibition of CdS photocorrosion. CO_2PR performed with CdS coupled with Bi_2S_3, having smaller bandgap energy than CdS, was also reported.[59] The Bi_2S_3/CdS nanocomposite fabricated with 15 wt% Bi_2S_3 exhibited the highest methanol production from CO_2 (6.13 mmol $g^{-1}\ h^{-1}$, Table 1 entry 3), which was at least 50% higher than those obtained with bare Bi_2S_3 (3.14 mmol $g^{-1}\ h^{-1}$) and CdS (2.01 mmol $g^{-1}\ h^{-1}$), under visible light irradiation. The enhanced photocatalytic activity suggested that the establishment of a heterojunction between CdS and Bi_2S_3 could improve charge separation and subsequently prolong the lifetime of photogenerated electron–hole pairs. Moreover, the surface area of the Bi_2S_3/CdS nanocomposite, which was 24–27 $m^2\ g^{-1}$, was slightly higher than those of the bare CdS and Bi_2S_3 (12 and 21 $m^2\ g^{-1}$, respectively). Hence, the synergetic effect of surface area and the heterojunction established between these two semiconductors had significantly improved the overall performance in CO_2PR. Increasing the specific surface area does not only provide more active sites for the photocatalytic reaction, but also affects the optical properties of the material. For instance, Jin *et al.* recently proposed that by increasing the length-to-width ratio of Bi_2S_3 nanoribbons, which increased the bandgap energy of Bi_2S_3 from 1.22 to 1.38 eV, the CH_3OH yield obtained was increased from 25.94 to 32.02 μmol $g_{catalyst}^{-1}\ h^{-1}$ under visible light irradiation ($\lambda \geq$ 420 nm).[61] However, the coupling of Bi_2S_3 nanoribbons with CdS was not demonstrated. Hence, it will be interesting to see the performance of Bi_2S_3 nanoribbons/CdS nanocomposites in the CO_2PR.

The coupling of CdS with other metal oxides, such as WO_3, has been demonstrated recently. For instance, Jin *et al.* proposed the coupling of WO_3 hollow spheres with CdS to form a hierarchical *Z*-scheme to increase the CO_2PR efficiency.[62] The coupling of WO_3–CdS had greatly enhanced the photoconversion of CO_2 to CH_4 to ~1.0 μmol $g_{catalyst}^{-1}\ h^{-1}$ under visible irradiation ($\lambda \geq$ 420 nm), whereas pristine WO_3 and CdS only produced trace amounts of CH_4.

Recently, the synthesis of $Zn_xCd_{1-x}S$ solid solutions has attracted extensive attention due to their versatility in tuning the band structures.[63–65] Moreover, the introduction of Zn can

Table 1 Photocatalytic CO_2 reduction yields obtained with various photocatalysts

No.	Photocatalyst	Product(s) of CO_2 photoreduction ($\mu mol\ g_{catalyst}^{-1}\ h^{-1}$)	Light source	Ref.
Sulphides				
1.	ZnS/montmorillonite nanocomposite	CH_4 1.17 CO 0.125	UV 8 W Hg lamp ($\lambda = 254$ nm)	49
2.	CdS wurtzite/zinc-blende nanohybrid	CO 1.61 CH_4 0.31	300 W Xe lamp ($\lambda \geq 420$ nm)	54
3.	Bi_2S_3/CdS	CH_3OH 6.13 mmol $g_{catalyst}^{-1}\ h^{-1}$	500 W Xe lamp ($\lambda \geq 320$ nm)	59
	CdS wurtzite/zinc-blende nanohybrid	CO 1.61 CH_4 0.31	300 W Xe lamp ($\lambda \geq 420$ nm)	54
4.	$Zn_xCd_{1-x}S$ solid solution and tetra(4-carboxyphenyl)porphyrin iron(III) chloride	CO 1.28 μmol	300 W Xe lamp (420 nm < λ <780 nm	58
5.	Cu_2S/CuS	CH_4 46.21 ± 6.50 $\mu mol\ m^{-2}\ h^{-1}$	A.M 1.5 simulated sunlight	60
6.	RuO_2-modified $Cu_xAg_yIn_zZn_kS_m$ solid solutions	CH_3OH 118.5	1000 W Xe lamp (λ > 400 nm)	69
Oxides				
7.	ZnO	CH_3OH 325	355 nm laser beam	74
8.	NiO	CH_3OH 388		
9.	Fluffy mesoporous ZnO	CO 0.73	8 W fluorescent tube (7 $mW\ cm^{-2}$)	75
10.	N-doped ZnO	CO 0.04		
11.	ZnO plates	CO 763.5 ppm $g_{catalyst}^{-1}\ h^{-1}$ CH_4 205.2 ppm $g_{catalyst}^{-1}\ h^{-1}$	300 W Xe arc lamp	76
12.	Ultralong and ultrathin single crystal Zn_2GeO_4 nanoribbons	CH_4 25	300 W Xe arc lamp	77
13.	Zn_2GeO_4 nanorods	CO 179 ppm $g_{catalyst}^{-1}\ h^{-1}$ CH_4 35 ppm $g_{catalyst}^{-1}\ h^{-1}$	300 W Xe arc lamp	78
14.	RuO_2 and Pt co-loaded $Zn_{1.7}GeN_{1.8}O$ nano-sheaves	~55	300 W Xe arc lamp (λ > 420 nm)	79
15.	$ZnGa_2O$ nanosheet-scaffolded microspheres	69	300 W Xe arc lamp with an IR cut filter	80
16.	Zn_2SnO_4 hexagonal nanoplates	47	300 W Xe arc lamp	81
17.	Ce-doped $ZnFe_2O_4$	CO ~20	Visible light	82
18.	Quasi-cubic WO_3	~0.34	300 W Xe lamp	83
19.	Ultrathin single crystal WO_3	~1.1	300 W Xe arc lamp	84
20.	Ultrathin $W_{18}O_{49}$	CH_4 2200	Full-arc Xe lamp	85
21.	Bi_2WO_6 nanosheets with well-defined {001} facets	1.1	300 W Xe arc lamp	86
22.	$BiWO_6$	CH_3OH 32.6	300 W Xe lamp (λ > 420 nm)	87
23.	$NaNbO_3$ nanowires	CH_4 653 ppm $g_{catalyst}^{-1}\ h^{-1}$	300 W Xe lamp	88
24.	KNb_3O_8 nanobelts	CO 3.58	350 W Xe lamp	89
25.	HNb_3O_8 nanobelts	CO 1.71		
26.	$SrNb_2O_6$ nanorods	CO 51.2	400 W Hg lamp	90
27.	3% NiO_x–Ta_2O_5-1% immobilised on reduced graphene	CH_3OH 197.92	400 W metal halide lamp	91
28.	Core–shell Ni/NiO-loaded N-$InTaO_4$	CH_3OH 160	Xe lamp (100 mW, 390 ≤ λ ≤ 770	92
29.	$LaTa_7O_{19}$	CO 50	400 W Hg lamp	93
30.	$CaTa_4O_{11}$	CO 70		
31.	1.0 wt% Ag-modified Ba-doped $NaTaO_3$	CO ~50	400 W Hg lamp	94
32.	$K_2YTa_5O_{15}$	CO 91.9	4000 W Hg lamp	95
33.	Ag-modified Ga_2O_3	CO 10.5	UV light	96
34.	Lamellar $BiVO_4$	CH_3OH 5.52	300 W Xe lamp (full spectrum)	97
35.	$CuGa_{1-x}Fe_xO$	CO ~9.2	300 W Xe arc lamp	98
36.	CoAl-layered double hydroxides	CH_4 4.2	500 W Xe lamp	99
Oxynitrides				
37.	Porous TaON	CH_3CHO 0.52 C_2H_5OH 2.03	300 W Xe lamp	100
38.	$ZnAl_2O_4$-modified $ZnGa_2ON$	CH_4 9.2	300 W Xe lamp ($\lambda \geq 420$ nm)	101
Nitrides				
39.	GaN	CO 1130 CH_4 1.3	300 W Xe lamp	102
40.	Rh/Cr_2O_3-decorated GaN nanowires	CO 120 CH_4 3.5		

manipulate the structure of the surface atoms in CdS, which influences the adsorption or desorption of the reactants, intermediates and products in photocatalytic reactions.[58] In a very recent study, Li *et al.* integrated the well-defined floccule-like $Zn_xCd_{1-x}S$ solid solution (Fig. 3) with tetra(4-carboxyphenyl)porphyrin iron(III) chloride for CO_2 photoreduction under visible light irradiation.[58] The optimised photocatalyst, which was synthesized with $Zn(NO_3)_2 \cdot 6H_2O$ and $Cd(NO_3)_2 \cdot 4H_2O$ at 0.25 : 0.75 (ZCS-1, Fig. 3), produced 1.28 μmol of CO with a selectivity of 93% after 4 h. However, pristine CdS and other synthesized $Zn_xCd_{1-x}S$ solid solutions produced less than 0.4 μmol of CO under visible light irradiation. The superior performance of ZCS-1 was attributed to the presence of sulphur vacancies that trapped photogenerated electrons, provided CO_2 adsorption sites and facilitated the interaction between the $Zn_xCd_{1-x}S$ solid solution and tetra(4-carboxyphenyl)porphyrin iron(III) chloride, resulting in efficient interfacial electron transfer for the subsequent photocatalytic reduction reaction.

Copper-based materials. $Cu_{2-x}S$, which have been shown to exhibit localised surface resonance in the near infrared region, and CuS, which has a direct bandgap of 2.0 eV, are nearly ideal for optimal sunlight absorption.[66,67] By carefully controlling the anodization voltage and temperature during the electrochemical anodization of copper foil and copper-coated Kapton substrates, in sodium sulphide electrolyte, copper sulphides with a nanowall nanostructure were obtained (Fig. 4).[60] The sample anodized with 1.5 V at 5 °C exhibited the highest methane formation in the CO_2PR (Table 1 entry 5) under the irradiation of simulated sunlight. At low voltage and temperature, sulphur diffusion was low, leading to a lower concentration of excess sulphur in the sample that yielded Cu_2S. As a result, less bulk Cu vacancy defects were formed within the sample. Cu_2S exhibited higher charge mobility than the CuS nanostructured array, which was obtained at high temperature and high voltage.

To engineer the bandgap energy of the photocatalyst that matches the solar spectrum, a solid solution with large and small bandgap semiconductors was proposed. For instance, Arai *et al.* used the Cu-based sulphide complex Cu_2ZnSnS_4 with a direct bandgap of 1.5 eV and a large optical absorption coefficient and obtained a high selectivity of the photoelectrochemical CO_2 reduction reaction (>80%).[68] The Cu-based sulphide complex reported by Liu *et al.* showcased that the Cu-based sulphide complex was able to reduce CO_2 under visible light irradiation in the presence of a Ru co-catalyst.[69] The Ru–$Cu_xAg_yIn_zZn_kS_m$ solid solutions induced the formation of methanol in CO_2PR under visible light irradiation (Table 1 entry 6). Although the study reported that the optimal performance could be obtained through the elemental composition manipulation, the nanostructures of the sulphide complex were not revealed. It is therefore questionable whether the efficiency of these photocatalysts could be further enhanced through the manipulation of their microstructures. Moreover, the stability of metal sulphates in most of the studies has not been demonstrated, and this should be emphasized more in future work.

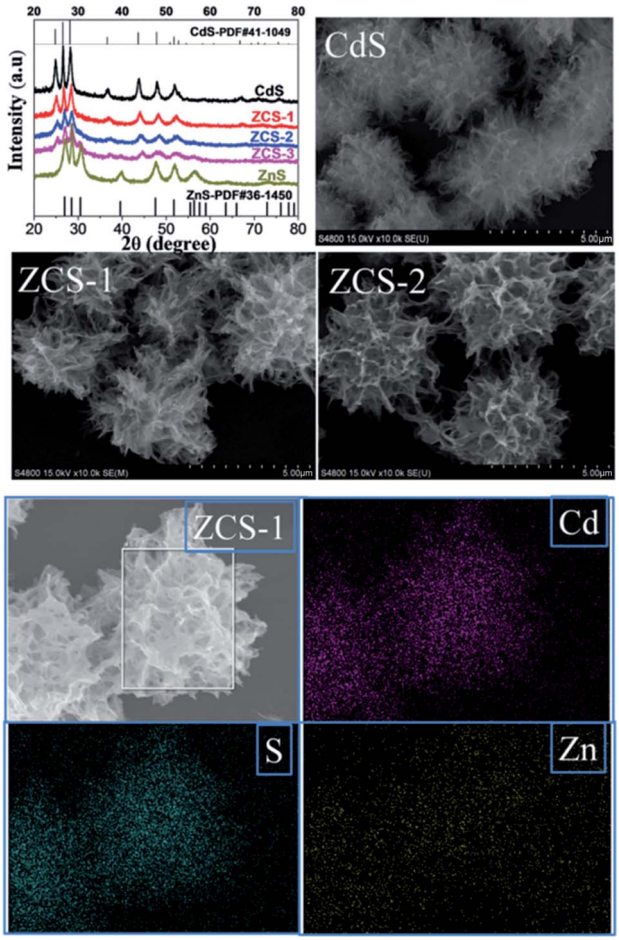

Fig. 3 XRD patterns, SEM images and EDX mapping of the synthesized CdS and $Zn_xCd_{1-x}S$ solid solutions. Reproduced from ref. 58 with permission.

2.2 Oxides

Semiconducting oxides have been widely used as photocatalysts because of their stability and resistance to photocorrosion under irradiation. Hence, oxides have been used for photooxidation and photoreduction reactions. The intrinsic properties of metal oxides play a critical role in determining their feasibility for CO_2PR. For example, CO_2PR was observed for p-type NiO covalently linked with a Zn porphyrin light-harvesting sensitizer and rhenium bipyridine system, whereas the CO oxidation reaction was observed when a similar system was coupled with n-type NiO.[70] There are two main groups of metal oxides with a closed-shell electronic configuration that have been at the centre of interest for a CO_2PR system. The first group includes octahedrally coordinated d^0 transition metal ions (Ti^{4+}, Zr^{4+}, Nb^{5+}, Ta^{5+}, V^{5+}, and W^{6+}). Apart from TiO_2, which is the most prominent member of this group, other binary oxides (*e.g.*, ZrO_2, Nb_2O_5, and Ta_2O_5) have been used in CO_2PR. A number of more complex oxides referred to as titanates, niobates, tantalates, *etc.*[71,72] are often found in a perovskite composite, AMO_3 (A = electropositive cation and M = transition metal; *e.g.*, $SrTiO_3$ and $NaNbO_3$), or in perovskite-related structures. Since

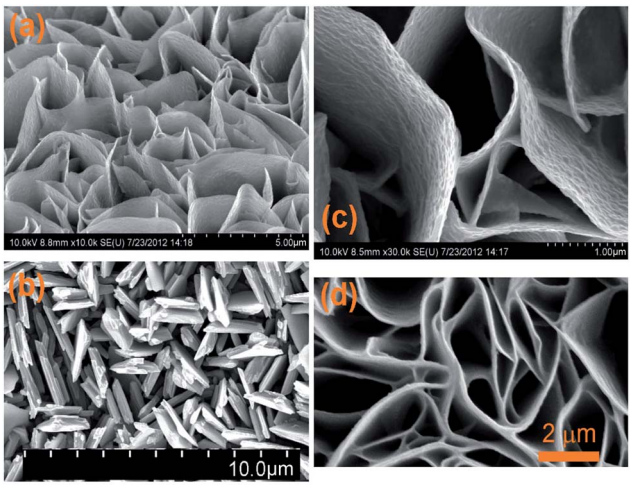

Fig. 4 SEM images of the copper sulphide nanowalls oriented vertically to the copper foil anodized at 1.5 V at room temperature (a and c), and 3.0 V (b) and 1.5 V (d) at 5 °C. Reproduced from ref. 60 with permission.

a recent published review has covered the use of perovskite oxide nanomaterials for CO_2 photoreduction,[73] this area will not be further discussed here. The second group includes main group metal oxides in a d^{10} configuration with a general formula of M_yO_z or A_xM_yO, where M represents Ga, Ge, In, Sn, or Sb. Many of these photocatalytically active binary and ternary oxides initially found application in photocatalytic water splitting, but they have very recently started to be utilised for CO_2PR.[73]

Zinc-based materials. ZnO has been widely used in the photodegradation of organic dyes and chemicals due to its direct and wide bandgap (3.37 eV).[103] Additionally, the bandgap and photocatalytic mechanism of ZnO are similar to those of TiO_2, and thus, ZnO was also used for CO_2PR. To compare the CO_2 photoreduction efficiency of ZnO with that of other commonly used wide bandgap semiconductors, Yahaya *et al.* employed commercially available TiO_2, ZnO and NiO as photocatalysts for CO_2 photoreduction under 355 nm UV laser irradiation.[74] Among the samples, ZnO and NiO produced high yields of methanol (325 and 388 μmol g^{-1} h^{-1} over 1.5 h, respectively, Table 1, entries 7 and 8); whereas TiO_2 had the lowest production yield. In order to enhance the light absorption of commercial ZnO in the UV-vis region, ZnO was calcined to 350 °C and the ZnO obtained was immobilised onto a stainless-steel mesh to reduce the agglomeration of the photocatalyst.[104] The maximum conversion of CO_2 achieved was 11.9% (*i.e.*, percentage of CH_4 produced from CO_2 in the presence of a CH_4 reductant). A study revealed that the microstructure of ZnO played a more vital role than doping of ZnO with nitrogen (N-ZnO), even though the latter showed enhanced light absorption from 400 to 650 nm.[75] A fluffy mesoporous structured ZnO with a surface area of 29.7 m^2 g^{-1} exhibited enhanced CO production (0.73 μmol $g_{catalyst}^{-1}$ h^{-1}, Table 1, entry 9) under UV-vis light irradiation when compared to the N-doped ZnO (1.2 m^2 g^{-1}, 0.04 μmol $g_{catalyst}^{-1}$ h^{-1}, Table 1, entry 10). A separate publication reported that ZnO plates with porous rectangular and assembled hexagonal morphologies (15.5 m^2 g^{-1}, which was about 2.6 times that of the commercial ZnO, Fig. 5) could be obtained by using $NH_4Zn_3(OH)_6NO_3$.[76] The synthesized ZnO plates exhibited a much higher production of CO and CH_4 (76.35 and 20.52 ppm h^{-1}, respectively) than the pristine hexagonal ZnO plates (44.68 and 1.57 ppm h^{-1} of CO and CH_4, respectively).

Doping has been widely used to extend the light absorption of wide bandgap semiconductors to a longer wavelength region by introducing intra-band states above the valence band. However, this approach tends to increase the recombination rate and decrease the charge mobility of the semiconductor, as discussed in Section 1. To avoid these drawbacks, the introduction of foreign cations into the binary semiconductor was considered instead of doping. For example, the ternary Zn_2GeO_4 semiconductor was used for CO_2PR under UV-vis irradiation. By fabricating ultralong and ultrathin single crystal Zn_2GeO_4 nanoribbons, the photocatalytic reduction rate of CO_2 into CH_4 was greatly enhanced to 25.0 μmol $g_{catalyst}^{-1}$ h^{-1} when compared to that of the bulk Zn_2GeO_4 (trace amounts, Table 1, entry 12).[77] The enhanced photocatalytic efficiency was attributed to the superb crystal quality and higher surface area (28.3 m^2 g^{-1}) when compared to the bulk Zn_2GeO_4 (0.75 m^2 g^{-1}), resulting in enhanced separation of photogenerated electron–hole pairs and charge mobility. In the following year, the same group proposed the synthesis of the single crystal Zn_2GeO_4 at 40 °C to optimise the surface area.[78] As a result, the surface area of the synthesized Zn_2GeO_4 nanorods was 33.1 m^2 g^{-1} which yielded 179 and 35 ppm $g_{catalyst}^{-1}$ h^{-1} of CO and CH_4, respectively. Further increasing the temperature to 100 °C, however, decreased the surface area to 14.8 m^2 g^{-1}, yielding only 3.2 and 0.4 ppm h^{-1} of CO and CH_4, respectively. By reducing the concentration of the Ge-precursor and the solvothermal time employed in the first study in 2010 (refer to ref. 77) by half, a sheaf-like superstructured Zn_2GeO_4 was obtained and reported by the same group in 2012 (Fig. 6).[79] Although the CO_2PR of the superstructured Zn_2GeO_4 was not reported in this study, the optimised RuO_2 and Pt co-loaded $Zn_{1.7}GeN_{1.8}O$ nano-sheaves after nitridation (32.33 m^2 g^{-1}) could produce CH_4 with an apparent quantum yield of 0.024% at 450 nm (Table 1 entry 14).

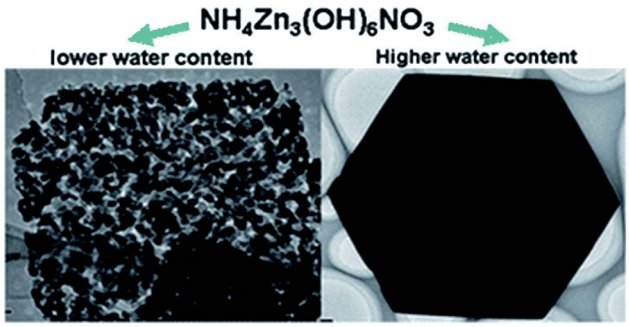

Fig. 5 ZnO synthesized from $NH_4Zn_3(OH)_6NO_3$ with <3 mL (left) and >3 mL (right) of water. Reproduced from ref. 76 with permission.

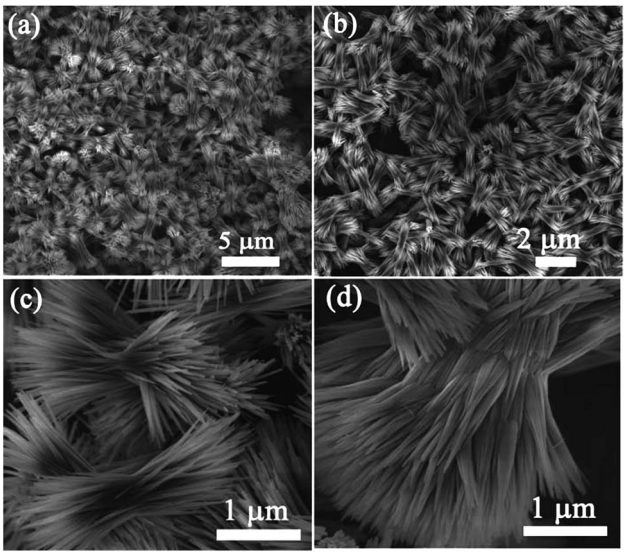

Fig. 6 SEM images of a sheaf-like Zn_2GeO_4 superstructure at different magnifications. Reproduced from ref. 79 with permission.

Other nanostructured ternary Zn-based oxides were also proposed by the same group more recently, including $ZnGa_2O$ nanosheet-scaffolded microspheres[80] and hexagonal nanoplate-textured Zn_2SnO_4 with micro-octahedron architecture for CO_2PR application.[81] The unique architecture of the synthesized $ZnGa_2O$ and Zn_2SnO_4 significantly enhanced the separation of photogenerated electron–hole pairs, increased the surface area and extended light absorption. Hence, the methane yield obtained from the CO_2PR was greatly improved from trace amounts to 69 and 47 ppm $g_{catalyst}^{-1}$ h^{-1} for the nanostructured $ZnGa_2O$ and Zn_2SnO_4, respectively (Table 1, entries 15 and 16).

To promote co-adsorption of CO_2 and H_2O, Guo *et al.* fabricated $ZnFe_2O_4$ spinels doped with Ce.[82] By using *in situ* FTIR, it was found that the CO_2 amount adsorbed on the surface of Ce-doped $ZnFe_2O_4$ was much higher than that on pristine $ZnFe_2O_4$. This phenomenon was attributed to the increase of basicity due to the presence of alkaline CeO_2 and electron density on the surface of the Ce-doped $ZnFe_2O_4$, thereby increasing the number of adsorption bonds between the CO_2 molecules and the surface of the photocatalyst, and activating the O=C bond (Fig. 7). The formation of active b-CO_3^{2-} and b-HCO_3^- species, which could be readily translated to highly valuable products in the CO_2 photoreduction, was detected. Recently, Xiao *et al.* discovered that ultrafine $ZnFe_2O_4$ nanoparticles with a high specific surface area (112.9 m^2 g^{-1}) could promote the selectivity of the photoproduction of CH_3CHO over CH_3CH_2OH, and they produced 57.8 and 13.7 μmol g^{-1} h^{-1}, respectively, under visible light irradiation (>400 nm).[105]

Tungsten-based materials. Among the first group of metal oxides, WO_3 has the smallest bandgap energy of 2.7 eV and as the edge of its conduction band is located at 0 V *vs.* NHE at pH 7, it cannot reduce CO_2.[4,106] However, Xie *et al.* found that when the architecture of the WO_3 changed from quasi-cubic with an equal percentage of {002}, {200} and {020} facets to rectangular sheet-like with dominant {002} facets, it could induce CO_2PR in

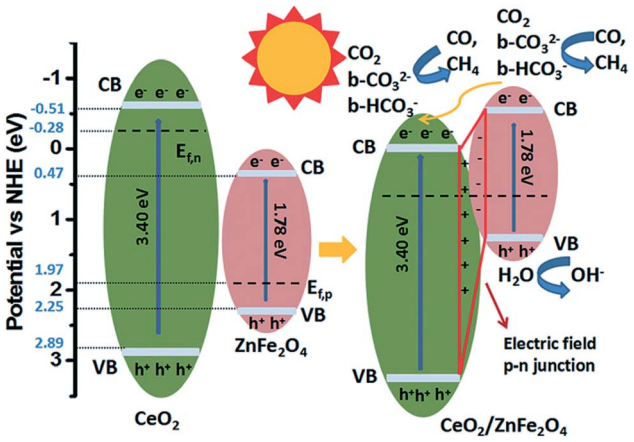

Fig. 7 Schematic of the mechanism of CO_2 photoreduction with H_2O vapour over $CeO_2/ZnFe_2O_4$. Reproduced from ref. 82 with permission.

the presence of H_2O.[83] The change of the predominantly exposed facets had a significant effect on the electronic configuration of WO_3, in which the rectangular sheet-like WO_3 possessed a slightly larger bandgap (2.79 eV) and its conduction band was increased by 0.3 eV. As a result, the conduction band was positioned slightly above the CH_4/CO_2 potential (−0.24 V), inducing the methane formation from CO_2 at a rate of ~0.34 μmol $g_{catalyst}^{-1}$ h^{-1}. Chen *et al.* found that the conduction band of WO_3 was shifted to a more negative position (−0.42 V, bandgap energy: 2.79 eV) with a stronger reducing driving force, when the ultrathin (~4–5 nm) single crystal WO_3 was synthesized using a solid–liquid phase arc discharge route in an aqueous solution.[84] The yield obtained from the CO_2PR was ~1.1 μmol $g_{catalyst}^{-1}$ h^{-1} under visible light irradiation (λ > 420 nm), whereas commercial WO_3 powder produced only trace amounts of methane under the same conditions. A high aspect ratio of ultrathin $W_{18}O_{49}$ exhibited extended optical properties in the visible and near infrared regions due to the presence of a large amount of oxygen vacancies (Fig. 8).[85] The synthesized

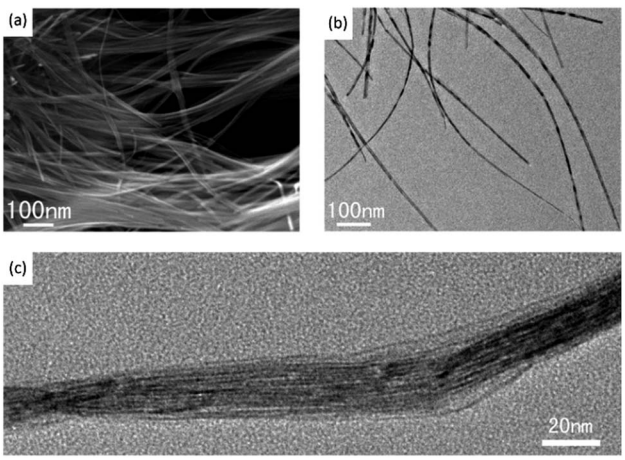

Fig. 8 SEM (a), TEM (b) and high resolution TEM (c) images of $W_{18}O_{49}$. Reproduced from ref. 85 with permission.

ultrathin $W_{18}O_{49}$ exhibited the photoreduction of CO_2 to CH_4 at 70 °C under visible light irradiation without a co-catalyst (Fig. 8, Table 1 entry 20). The study observed that the selectivity towards CH_4 over other hydrocarbons (*e.g.*, ethanol and acetone) was as high as 95%.

The introduction of foreign elements into tungsten oxide, which generated ternary Bi_2WO_6, was reported.[86] The Bi_2WO_6 with predominant {001} facets was proposed to be the most energetically favoured reactive surface for CO_2 dissociation, resulting in 1.1 μmol $g_{catalyst}^{-1}$ h^{-1} of methane under visible light irradiation (λ > 420 nm), whereas the bulk Bi_2WO_6 prepared through a solid state reaction produced only trace amounts of methane. Cheng *et al.* also proposed that the microstructure of Bi_2WO_6 could enhance CO_2 adsorption.[87] A template-free anion exchange strategy was used to synthesize hollow microspheres of Bi_2WO_6 (Fig. 9a and b). The synthesized Bi_2WO_6 exhibited higher CO_2 adsorption capacity when compared to $BiVO_4$ and $BiPO_4$ nanoparticles without hollow structures (Fig. 9c and d, respectively), leading to high photoconversion of CO_2 into methanol.

Niobate-based materials. Niobates with a perovskite structure have gained some attention because they share many characteristics (*i.e.*, non-toxicity, stability, and indirect wide bandgap) with titanates. Moreover, the conduction band of niobates is slightly more reductive than that of titanates, suggesting that niobates could be a more suitable material for CO_2PR. A study had shown that the microstructure of $NaNbO_3$ played an important role in its photocatalytic activity. $NaNbO_3$ nanowires (653 ppm h^{-1} g^{-1}, Fig. 10a) with a smaller bandgap (3.2 eV) and larger surface area (12.0 m^2 g^{-1}) exhibited much higher methane formation from CO_2 when compared to the $NaNbO_3$ bulk (3.2 eV, 1.4 m^2 g^{-1}, 22 ppm h^{-1} g^{-1}, Fig. 10b).[88] The enhanced photocatalytic activity was proposed to be due to the high crystallinity, high aspect ratio and anisotropic effect of the synthesized nanowires. Li *et al.* also demonstrated that the size and microstructure of photocatalysts play an important role in their photocatalytic activity.[89] KNb_3O_8 and HNb_3O_8 nanobelt samples with a higher surface area, which were 28.8 and 39.4 m^2 g^{-1}, respectively, exhibited a ≥10 times higher photoproduction rate of methane from CO_2 than the irregularly shaped KNb_3O_8 and HNb_3O_8 samples, which were 2.7 and 6.5 m^2 g^{-1}, respectively (Table 1 entry 24 and 25). A similar observation was reported by Xie *et al.*, in which the nanoplates of $SrNb_2O_6$ with an increased surface area revealed improved chemisorption of CO_2 and the separation of photogenerated electron–hole pairs.[107] As a result, more products, such as CO and CH_4, were obtained from the CO_2PR compared to the $SrNb_2O_6$ nanorods and nanoparticles with a lower surface area. A more recent study revealed that the nanorod-structured $SrNb_2O_6$ (1.78 m^2 g^{-1}, 51.2 μmol $g_{catalyst}^{-1}$ h^{-1}) exhibited a higher photoreduction rate and selectivity towards CO evolution over H_2 (>95%) than the $SrNb_2O_7$ nanoflakes (3.85 m^2 g^{-1}, 6 μmol $g_{catalyst}^{-1}$ h^{-1}, ~39%) and $SrNb_2O_6$ nanoparticles even though the latter possessed a higher surface area.[90] This phenomenon was attributed to the separation of the reduction and oxidation sites on the nanorods that decreased the recombination of photogenerated electron–hole pairs.

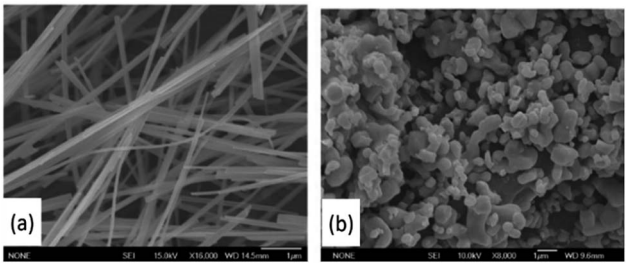

Fig. 10 $NaNbO_3$ nanowires (a) and bulk particles (b). Reproduced from ref. 88 with permission.

Tantalum-based materials. Tantalum-based semiconductors have been widely used as a photocatalyst for water splitting. Having higher potentials than TiO_2 and above the reduction potential of CO_2/CH_3OH, H_2CO_3/CH_3OH, HCO_3^-/CH_3OH and CO_3^{2-}/CH_3OH, Ta_2O_5 can be employed for the CO_2PR.[92] However, the large bandgap energy of Ta_2O_5 (~3.9 eV) has restricted its light absorption in the visible region.[108] Hence, Sato *et al.* used N-Ta_2O_5 to couple a series of ruthenium bipyridine catalysts for the photocatalytic CO_2 reduction to formic acid under visible light irradiation (405 nm).[109] The production rate was found to be ~70 μmol $g_{catalyst}^{-1}$ h^{-1} in an acetonitrile/triethanolamine mixture. To enhance the electron transportation and suppress the electron–hole recombination, Ta_2O_5 was immobilised on reduced graphene and NiO_x was used as the co-catalyst (Fig. 11).[91] The highest photoproduction rate of methanol from 3% NiO_x–Ta_2O_5-1% reduced graphene sample was ~20.83 and 197.92 μmol $g_{catalyst}^{-1}$ h^{-1} without and with the presence of $NaHCO_3$ solution, respectively.

Much effort has focused on $InTaO_4$ as the ternary tantalum-based semiconducting photocatalyst for CO_2PR. For instance, Pan and Chen demonstrated that $InTaO_4$ could reduce CO_2 to methanol (~1.1 μmol $g_{catalyst}^{-1}$ h^{-1}) in 0.2 M $KHCO_3$ aqueous solution under visible light irradiation.[110] The methanol production rate could marginally increase to 1.2 μmol $g_{catalyst}^{-1}$

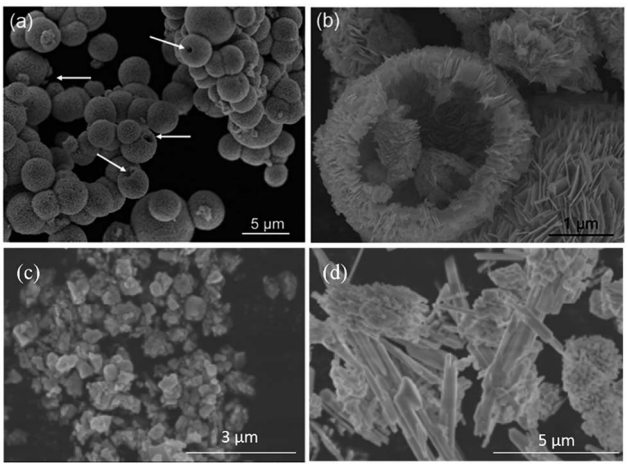

Fig. 9 SEM images of Bi_2WO_6 hollow microspheres (a and b), $BiVO_4$ (c) and $BiPO_4$ (d) reproduced from ref. 87 with permission.

h^{-1} after coupling 1 wt% NiO as the co-catalyst and 1.4 μmol $g_{catalyst}^{-1}$ h^{-1} after the application of reduction–oxidation pre-treatment. Tuning the size and crystallinity of $InTaO_4$ nanoparticles resulted in the bandgap energy range from 2.6 to 3.0 eV and could also enhance the production of methanol from CO_2.[111] The highest production rate was about 2.7 μmol $g_{catalyst}^{-1}$ h^{-1} when 1.0 wt% NiO was added as the co-catalyst. The methanol generation from $InTaO_4$ was further enhanced by introducing core–shell Ni/NiO nanoparticles on nitrogen doped $InTaO_4$, leading to 160 μmol $g_{catalyst}^{-1}$ h^{-1} under the irradiation of light with wavelengths ranging from 390 to 770 nm.[92] $KTaO_3$ was also used to reduce CO_2 to CO under visible light irradiation.[112] Three samples were synthesized with different bandgaps ranging from 3.5 to 3.7 eV and yielded the highest amount of CO at ~62 ppm $g_{catalyst}^{-1}$ h^{-1}.

Recently, $LaTa_7O_{19}$ and $CaTa_4O_{11}$ (bandgap energies of 4.1 and 4.5 eV, respectively) were shown to be active for CO_2PR. CO was produced after loading with 1 wt% Ag co-catalyst due to the preferable conduction band positions (50 and 70 μmol $g_{catalyst}^{-1}$ h^{-1}, respectively, in the presence of 0.1 M $NaHCO_3$ under the irradiation of a 400 W high-pressure mercury lamp).[93] $NaTaO_3$ doped with different elements, such as Mg, Ca, Sr, Ba and La, has been proposed as a highly active photocatalyst for CO_2PR using water as the electron donor in the presence of a Ag co-catalyst under UV irradiation.[94] Among the samples, Ba-doped $NaTaO_3$ loaded with 1.0 wt% Ag co-catalyst using the liquid-phase reduction method exhibited the highest CO production and selectivity from CO_2 (~50 μmol $g_{catalyst}^{-1}$ h^{-1} and 56%, respectively).

Quaternary tantalates have been developed recently and revealed to be active for CO_2 photoreduction in the presence of water.[113] $K_2RETa_5O_{15}$ (RE = rare-earth element, namely La, Ce, Pr, Nd, Y, and Sm) was fabricated using the flux method with KCl, which favoured the rod-like morphology, followed by calcination treatment at 1150 °C for 6 h.[95] Among the quaternary tantalates, $K_2CeTa_5O_{15}$ possessed the smallest bandgap energy (2.42 eV, 0.7 μmol $g_{catalyst}^{-1}$ h^{-1}), but $K_2YTa_5O_{15}$ photoproduced the highest amount of CO (3.86 eV, 91.9 μmol $g_{catalyst}^{-1}$ h^{-1}). The addition of Y was shown to be beneficial for capturing CO_2 and subsequently for photoreduction. Meanwhile, the presence of K in the tantalates played an important role in determining the growth orientation of the rod-like structure, thereby affecting the activity in CO_2 photoreduction.

Miscellaneous. CeO_2 is a basic metal oxide that can transform inert linear CO_2 to b-HCO_3^- and b-CO_3^{2-} to reduce the reductive potential of CO_2.[114] Hence, it has recently attracted a lot of attention. However, it suffers from rapid recombination of photogenerated electron–hole pairs and possesses a large bandgap (3.0–3.4 eV), which restricts the light absorption in the UV range.[115] To improve the performance of CeO_2 for the photocatalytic reduction of CO_2 under visible irradiation, Xiong *et al.* proposed the coupling of Ag/Ag_3PO_4 with CeO_2 to construct heterojunctions for enhancing the separation of photogenerated electron–hole pairs and improve light absorption because Ag_3PO_4 has a narrow bandgap of 2.42 eV.[116] The highest CH_3OH and C_2H_5OH yield obtained was 10.6 and 7.9 μmol $g_{catalyst}^{-1}$ h^{-1}, respectively. Zhang discovered that when Ni was loaded on CeO_2, the nanocomposite exhibited enhanced photo(thermo)catalytic performance and inhibited carbon deposition.[117] Moreover, it is interesting to note that the full light spectrum response from UV to infrared of the Ni metal on CeO_2 decreased the activation energy of C and CH oxidation steps, thus improving the overall photo(thermo)catalytic performance.

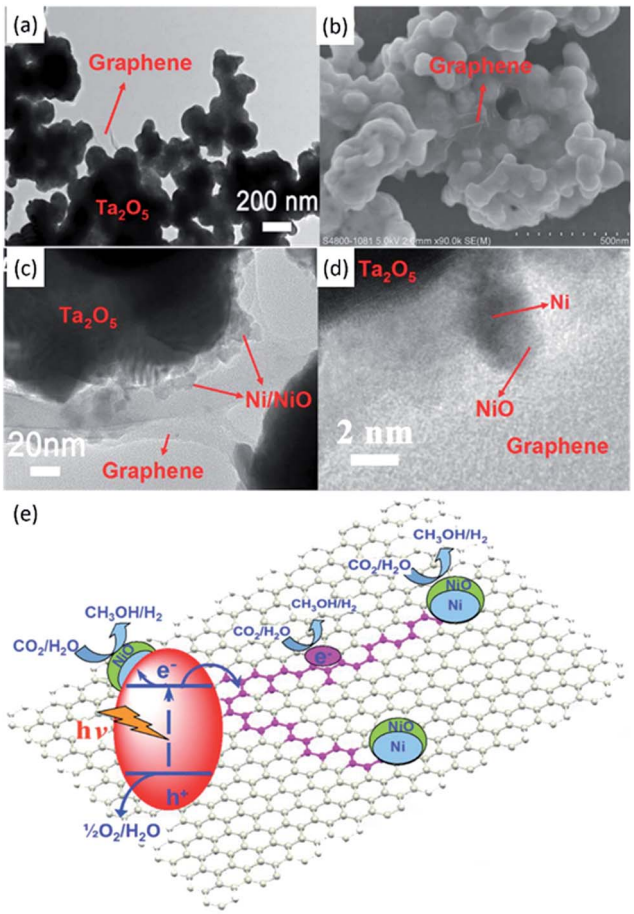

Fig. 11 TEM (a) and SEM (b) images of Ta_2O_5 immobilised on reduced graphene. TEM (c) and SEM (d) images of the NiO_x–Ta_2O_5-reduced graphene composite. Schematic illustration of the charge separation and transfer in the Ta_2O_5-reduced graphene system under UV-vis light (e). Reproduced from ref. 91 with permission.

MgO was employed to photocatalytically reduce CO_2 into CO with a production rate of ~1.6 μmol g^{-1} h^{-1} over 6 h in the presence of H_2 as the reductant under UV light (λ < 290 nm).[118] Mesoporous Ga_2O_3 yielded 1.46 and 0.21 μmol g^{-1} h^{-1} of CO and CH_4, respectively, from CO_2 under visible light irradiation.[119] When Ga_2O_3 was loaded with Ag, the photoproduction rate of CO from CO_2 was 10.5 μmol g^{-1} h^{-1} under UV light irradiation (Table 1 entry 33).[96] Iron oxides were proposed as a photoactive centre to induce the photocatalytic reduction of CO_2.[120] Using electron spin resonance spectroscopy (ESR), the photogenerated electrons from the Fe–O species were efficiently consumed by CO_2 under UV irradiation.

Lamellar $BiVO_4$ was proposed to exhibit a selective methanol production from CO_2 photoreduction under visible light

irradiation.[97] The maximum CH_3OH production rate was 5.52 μmol h^{-1} when 0.2 g of $BiVO_4$ was suspended in 100 mL of NaOH (1.0 M) under full spectrum irradiation of a Xe lamp. The photocatalytic mechanism was proposed according to which the Bi^{3+} sites could efficiently receive electrons from the V 3d-block bands of the $BiVO_4$ to form $CO_2^{\bullet-}$ radical anions, leading to the formation of methoxyl radicals ($\cdot OCH_3$) and eventually CH_3OH after hydrogen abstraction. Wang *et al.* doped the atomically thin layers of $BiVO_4$ with different percentages of Co.[121] The Co-doped $BiVO_4$ exhibited an efficient and stable activity for CO_2 photoreduction to CH_4. The optimal CH_4 production rate was 23.8 μmol g^{-1} h^{-1}, which was three times higher than that of the pristine $BiVO_4$, at 60 °C with an atmospheric CO_2 concentration (~400 ppm) under a UV lamp (25 W at 254 nm). The enhancement of the production rate of the Co-doped $BiVO_4$ was suggested to be due to the presence of electron enriched adsorption sites, which was contributed by the Co dopant, activating the CO_2 molecules for further reduction reaction.

Delafossite materials with a general stoichiometry of ABO_2, in which A is a monovalent metal ion, such as Cu, Ag, and Pt, and B is a trivalent metal ion, such as Al, Ga, and Fe, as the new class of photocatalysts have also been considered for CO_2PR.[98] $CuGaO_2$ (bandgap energy ~3.7 and weak absorption at 2.6 eV) and the Fe-alloyed $CuGa_{1-x}Fe_xO$ (1.5 eV) facilitated the photogeneration of CO from CO_2 under the irradiation of a Xe lamp though varied amounts of Fe substituted into $CuGaO_2$ did not significantly enhance the CO_2 photoreduction performance (Table 1 entry 35).[98]

Based on the Lewis acidity of CO_2, alkaline catalysts will benefit the adsorption and activation of CO_2. Layered double hydroxide (LDH) materials usually possess high specific surface areas, which provide numerous active sites for the catalytic reaction. The fabricated CoAl LDH facilitated an enhanced CO_2 photoreduction reaction when compared to P25 due to the surface alkaline OH groups for efficient adsorption of CO_2 at a low concentration.[99] The utilisation of LDH in CO_2 photoreduction has been reviewed previously, and thus, interested readers may refer to the published review articles.[40,122]

In summary, metal oxides have shown their ability to promote photocatalytic reduction of CO_2, as discussed in the previous section. However, most of these photocatalysts only work under UV irradiation due to their large bandgap energies (>3 eV). The relatively large bandgap of metal oxides originates from the valence band maximum, which is formed by O 2p orbitals and is more positive than 3 V.[123] Hence, if metal oxides meet the thermodynamic requirement for CO_2PR and H_2O photooxidation, then the bandgap of the metal oxides inevitably becomes larger than 3.0 eV, which is too wide to absorb visible light.[124]

2.3 Oxynitrides

Tantalum-based materials. The N 2p orbital has a higher potential energy than the O 2p orbital, which indicates that metal oxynitrides as well as metal nitrides could be employed as an efficient photocatalyst.[42,125] For example, in the case of tantalum oxynitride and tantalum nitride, when nitrogen-based N 2p atomic orbitals were introduced into Ta_2O_5, new orbitals with a higher bound state energy are generated, resulting in a decrease of bandgap energy.[42,108,126] As a result, the bandgaps of TaON and Ta_3N_5 (2.5 and 2.1 eV, respectively) are both smaller than that of Ta_2O_5 (3.9 eV) and thus can effectively absorb visible light and drive the photocatalytic activity. Moreover, the N content plays an important role in determining the bandgap energy in oxynitrides and nitrides. Therefore, Gao *et al.* proposed a Ca-assisted urea synthesis method to controllably synthesise TaON and Ta_3N_5 with a tailored N composition.[127] In addition, the initial urea : Ta molar ratio used in the proposed synthesis method was also beneficial to control the size and homogeneity of the final product. Recently, the use of the porous spherical architecture of TaON for CO_2 photoreduction was proposed.[100] The surface area of the porous spherical TaON was ~11.12 m^2 g^{-1}, whereas that of commercial TaON was ~7.41 m^2 g^{-1}. As a result, the CH_3CHO and C_2H_5OH production rates from CO_2 using the porous TaON (0.52 and 2.03 μmol $g_{catalyst}^{-1}$ h^{-1}) were higher when compared to those of the commercial TaON (0.16 and 0.84 μmol $g_{catalyst}^{-1}$ h^{-1}) under visible light irradiation. The enhanced CO_2PR in the porous TaON was attributed to the increase of surface area. In addition, the reduction of charge transfer distance and enhanced light scattering within the porous spherical structure were also suggested to play roles in enhancing the photocatalytic reduction of CO_2.

The CO_2PR is a multi-electron process, and a variety of products can be produced using a single semiconducting photocatalyst. The achievement of efficient and selective production of highly valuable fuels is critical for viable CO_2 photoreduction processes. The application of perovskite oxynitrides, such as $CaTaO_2N$ coupled with the binuclear Ru(II) complex photosensitiser and loaded with the Ag co-catalyst, revealed an enhanced selectivity for HCOOH production (>99%) from CO_2 under visible light irradiation due to the enhanced interfacial electron transfer.[128] A similar approach with the same photosensitiser and co-catalyst coupled with yttrium–tantalum oxynitride (YTON) was recently proposed by the same group.[129] The YTON (2.1 eV) exhibited a smaller bandgap than $CaTaO_2N$ (2.5 eV), thus extending the light absorption up to 600 nm. Moreover, the selectivity for HCOOH formation from CO_2 was not affected and remained as high as that in their previous study (>99%).

Zinc-based materials. Mesoporous ZnGeON was used as a photocatalyst for CO_2PR under visible light irradiation (λ < 400 nm).[130] The prolonged nitridation time from 1 to 15 h decreased the Zn and O contents, in which Zn was evaporated and O was substituted by N, at 800 °C in an NH_3 environment. However, the crystallinity of ZnGeON was enhanced with a slight decrease in the surface area. The ZnGeO nitrided for 10 h (24.4 m^2 g^{-1}) exhibited the highest CH_4 production rate of 2.7 ppm $g_{catalyst}^{-1}$ h^{-1}, which was higher than those of the ZnGeON prepared using the solid-state reaction (3.3 m^2 g^{-1}, 1.1 ppm $g_{catalyst}^{-1}$ h^{-1}) and N-doped TiO_2 (2.2 ppm $g_{catalyst}^{-1}$ h^{-1}). As discussed in Section 2.2, zinc-based materials like $ZnGa_2O_4$ possessed a bandgap energy of ~4.5 eV, in which

the valence band was mainly composed of O 2p and the conduction band was formed from the hybridization of Ga 4s and Zn 4p orbitals.[80,101] In order to reduce the bandgap energy, nitridation of mesoporous $ZnGa_2O_4$ was proposed. The nitridation of $ZnGa_2O_4$ stimulated the hybridization of Zn 3d, N 2p and O 2p and formed the valence band, whereas the conduction band was composed of the Ga 4s and 4p orbitals.[101] As a result, the bandgap energy was reduced to 2.5 eV, resulting from the uplifting of the maximum of the valence band and lowering of the minimum of the conduction band. To further enhance the CO_2PR performance, a $ZnGa_2ON$ solid solution was modified with $ZnAl_2O_4$ that acted as the CO_2 arrester (Fig. 12).[101] The increase of Zn content had also decreased the bandgap energy to 2.3 eV. Benefiting from the mesoporous structure, smaller bandgap and enhanced CO_2 adsorption ability, the $ZnAl_2O_4$-modified $ZnGa_2ON$ showed a methane generation rate of 9.2 μmol $g_{catalyst}^{-1}$ h^{-1} from CO_2, which was 9 times higher than that of the pristine $ZnGa_2ON$ under visible light irradiation ($\lambda \geq 420$ nm).

2.4 Nitrides

Gallium-based materials. Through engineering the nanostructure of the co-catalyst used, selectivity using semiconducting nitrides could be enhanced dramatically, as demonstrated by AlOtaibi *et al.*[102] The decoration of the nonpolar GaN nanowires with the Rh core and amorphous Cr_2O_3 shell co-catalyst significantly increased the production rate of CH_4 from 1.3 (bare GaN) to 3.5 μmol $g_{catalyst}^{-1}$ h^{-1}, but the CO production rate decreased from 1130 (bare GaN) to ~120 μmol $g_{catalyst}^{-1}$ h^{-1} in 24 h (Fig. 12). Due to the effective collection of photogenerated electrons by the Rh core and amorphous Cr_2O_3 shell co-catalyst, no apparent reductive reaction (*e.g.*, photoreduction of CO_2 to CO) occurred on the surface of GaN without Rh coverage. As a result, the product selectivity towards CH_4 was enhanced in the CO_2PR under UV-visible light irradiation. In addition, the decoration of the GaN nanowires with Rh/Cr_2O_3 could suppress the back reaction that formed H_2O from H_2 and O_2, and offered adsorption sites for CO_2.

In summary, both metal oxynitrides and nitrides have shown their capability to photoreduce CO_2 with more favourable optical properties when compared to metal oxides. Unfortunately, these groups of materials have not been extensively explored.

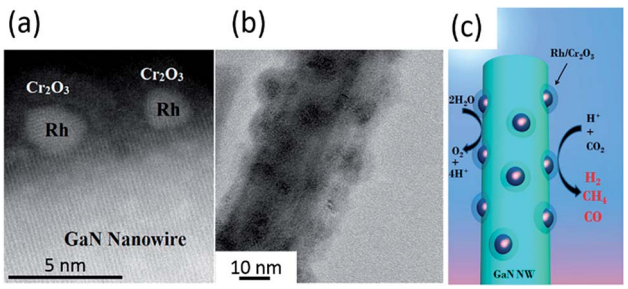

Fig. 12 (a) High-resolution TEM image and (b) TEM image of Rh/Cr_2O_3 core/shell decorated GaN nanowires. (c) Schematic of the photoreduction processes of CO_2 on Rh/Cr_2O_3-decorated GaN nanowires. Reproduced from ref. 102 with permission.

3. Hole scavengers for CO_2 photoreduction

Various semiconducting materials have been proposed as photocatalysts for CO_2PR under UV and/or visible irradiation, as discussed in Section 2 and summarised in some other references.[7–10,103,131] However, the quantum efficiency of the CO_2 photo-conversion into hydrocarbons remained low and could not rely only on the development of photocatalysts. System optimisation plays an important role in optimising the conversion rate and selectivity as well as photocatalyst stability. Therefore, the increase of CO_2PR efficiency through the introduction of a hole scavenging agent has gained significant interest. In this section, the use of organic and inorganic hole scavengers is reviewed.

3.1 Inorganic hole scavengers

As discussed in Section 2.1, metal sulphides suffer from photocorrosion in an aqueous dispersion due to the oxidation of lattice S^{2-} ions to elemental S and subsequently to sulphates.[51] Hence, the addition of reducing agents to prevent the oxidation of the lattice S^{2-} ions by scavenging the photogenerated holes was proposed. Kanemoto *et al.* achieved a cumulative quantum yield of 72% with irradiation of UV light at 313 nm (*i.e.*, 75.1 and 1.7 μmol $g_{catalyst}^{-1}$ h^{-1} of HCOOH and CO, respectively) when NaH_2PO_2 and Na_2S (0.35 and 0.24 M, respectively) were added into the system that contained ZnS as the photocatalyst for CO_2PR (Table 2 entry 1).[132]

A systematic study was recently carried out to investigate the effect of Na_2S as the hole scavenger for ZnS on the CO_2PR at $\lambda = 345$ nm.[133] The study elucidated that the photogenerated holes on the surface of ZnS were directly consumed by Na_2S, whereas photogenerated electrons were pumped into the conduction band simultaneously. In addition, the behaviour of the reaction rate at different pH values resembled that of the solubility of CO_2, discarding the direct participation of the HCO_3^- and CO_3^{2-} in the photoreduction process. This observation was supported by a very recent study, in which $KHCO_3$ was used as the hole scavenger in an aqueous system with ZnS.[134] The study demonstrated that $KHCO_3$ acted as an effective hole scavenger as well as a buffer to mitigate the pH change induced by the CO_2 saturation. This phenomenon, however, was not observed when only K_2SO_3 was used as the hole scavenging agent.

The optimised solution with 0.1 g of colloidal ZnS, 0.1 M K_2SO_3 and 0.5 M $KHCO_3$ achieved 464.2 and 81.3 μmol of HCOOH and CO, respectively, under UV-vis irradiation (Table 2 entry 2).[134] The selectivity towards HCOOH was reported to be 12.5%, and this could be improved to 95.0% when Cd was added to the colloidal ZnS suspension as the co-catalyst.

Inorganic salts (*e.g.*, NaOH, Na_2S, *etc.*) have been reported to have a significant effect on CO_2PR.[97,132,134,135] The addition of NaOH had been shown to increase the solubility of CO_2 compared to pure H_2O because the OH^- ions provided by NaOH in aqueous solution reacted with the dissolved CO_2, and transformed into CO_3^{2-} and further into HCO_3^- in the CO_2 saturated system.[136] It was suggested that the high

Table 2 Photocatalytic CO_2 reduction yields obtained by various photocatalyst after adding hole scavenger(s)

No.	Photocatalyst	Hole scavenger	Function/role	Product(s) of CO_2 photoreduction ($\mu mol\ g_{catalyst}^{-1}\ h^{-1}$)	Ref.
Inorganic					
1.	ZnS quantum crystallites	0.70 M NaH_2PO_2	Electron donor	HCOOH 75.10	132
		0.48 M Na_2S	Sulphur vacancy suppressor	CO 1.70	
2.	ZnS	0.1 M K_2SO_3	Hole scavenger	HCOOH ~250.00	134
		0.1 M $K_2SO_3^+$	Electron donor		
		0.5 M $KHCO_3$	Buffer solution	HCOOH 580.30	
3.	Zn-doped Ga_2O_3	0.1 M $NaHCO_3$	Hole scavenger	CO 117.00	138
4.	Ag-loaded $SrNb_2O_6$	0.1 M $NaHCO_3$	CO_2 supply	CO ~4.00	71
5.	Ag-loaded $Sr_2Nb_2O_7$			CO ~38.40	
6.	Sr and Ag co-loaded $NaTaO_3$	0.1 M $NaHCO_3$	Buffer for supplying CO_2	CO ~352.00	94
7.	Ni-Al layered double hydroxides (LDHs)	0.1 M NaCl	Hole scavenger	CO 112.80	139
8.	$BiVO_4$	1.0 M NaOH	Hole scavenger	CH_3OH 5.52	97
Organic					
9.	CdS	Acetonitrile + dichloromethane	Surface modifier	$(CH_3)_2CO$ ~0.24 μmol with 70 μM of CdS powder	140
			Surface modifier		
		1.0 mol dm^{-3} 2-propanol	Hole scavenger	$(CH_3)_2CO$ ~0.19 μmol with 70 μM of CdS powder	
10.	Wurtzite-ZnS	Isopropanol	Hole scavenger	HCOOH ~40 ppm $g_{catalyst}^{-1}\ h^{-1}$	141
		Ethylene glycol	Hole scavenger	HCOOH ~90 ppm $g_{catalyst}^{-1}\ h^{-1}$	
11.	Mononuclear Ru complex/C_3N_4	4 : 1 of *N*,*N*-dimethylacetamide (DMA) : triethanolamine (TEOA)	Proton quencher Electron donor	HCOOH ~1100.00	142
12.	Bi-nuclear Ru complex/Ag-loaded C_3N_4	4 : 1 of *N*,*N*-dimethylacetamide (DMA) : triethanolamine (TEOA)	Proton quencher Electron donor	HCOOH ~2115.00	143
13.	Bi-nuclear Ru complex/Ag-loaded C_3N_4	1.0 mM ethylenediaminetetraacetic acid disodium salt dihydrate, EDTA·Na_2	Electron donor	HCOOH ~31.67	144
14.		1.0 mM ethylenediaminetetraacetic acid disodium salt dihydrate (EDTA·Na_2) + 0.1 M K_2CO_3	Electron donor Surface modifier	HCOOH ~83.33	

concentration of HCO_3^- present in the system could accelerate the photoreduction reaction, thereby enhancing the photoreduction performance.[136,137] The direct consumption of HCO_3^{2-} to produce CO was observed in a CO_2 aqueous solution using a Zn-doped Ga_2O_3 photocatalyst.[138] This observation was further investigated by Nakanishi *et al.*, in which the production of CO occurred after transforming HCO_3^- into CO_2.[94] Therefore, the addition of HCO_3^- increased the CO_2 supply in the aqueous system, but did not enhance the numbers of reacted electrons and holes. In other words, under basic conditions, H_2 production could be significantly suppressed, resulting in a high selectivity of CO from CO_2. Jin *et al.* concurred that the addition of NaOH promoted the formation of HCO_3^-; however, the production of methanol was observed in the photocatalytic system with a $BiVO_4$ photocatalyst.[97]

The addition of NaOH, Na_2CO_3 and $NaHCO_3$ to the CO_2 photoreduction aqueous solution was shown to promote the photoproduction of CO, whereas H_2SO_4 and NaCl were found to favour water splitting, leading to the production of H_2.[90,94,136,137] However, a recent study has proposed that the inclusion of Cl^- from NaCl could scavenge the photogenerated holes for the CO_2 photocatalytic reduction process in a aqueous solution over Ni–Al layered double hydroxides.[139] The selectivity towards CO over H_2 was 86% when NaCl was added into the photoreduction system (~6.95 and ~1.16 μmol $g^{-1}\ h^{-1}$ of CO and H_2, respectively), whereas in the absence of a scavenging agent, the selectivity towards CO over H_2 was only 54% (~3.15 and ~2.63 μmol $g^{-1}\ h^{-1}$ of CO and H_2, respectively). The authors also pointed out that the addition of $NaHCO_3$ and Na_2CO_3 promoted the production of H_2 *via* the reduction of H^+ derived from H_2O instead of the CO_2PR. Neither Na_2SO_4 nor $NaNO_3$ could positively enhance the production of CO. A similar extent of CO evolution and selectivity were also observed when other chloride salts were added, namely CsCl (~8 μmol $g^{-1}\ h^{-1}$ of CO, 82%), $MgCl_2$ (~7 μmol $g^{-1}\ h^{-1}$ of CO, 82%) and $CaCl_2$ (~7.5 μmol $g^{-1}\ h^{-1}$ of CO, 82%). However, other halogenide salts (NaBr and NaI) showed a weaker photoreduction ability than NaCl.

3.2 Organic hole scavengers

Since the last century, ZnS had been used as photocatalyst for the CO_2PR.[146,147] Triethylamine (TEA) showed its feasibility to be used as the hole scavenger, inhibiting the photocorrosion for sulphite photocatalysts.[7] In ZnS systems, 2-propanol was one of

the common hole scavengers for CO_2PR. A previous report proposed that the light energy could be stored within the light-induced reaction given as

$$CO_2 + (CH_3)_2CHOH \rightarrow HCOOH + (CH_3)_2CO$$

The Gibbs free energy of this reaction is +62.8 kJ mol^{-1} at 25 °C.[147]

In a system of Cd-loaded ZnS, CO_2 photoproduced formic acid with a quantum efficiency 32.5% in the presence of 1 M 2-propanol.[147] Further increasing the Cd concentration resulted in the formation of CO. A study revealed that CdS was capable of photoreducing CO_2 to CO when *N*,*N*-dimethylformamide (DMF) containing 1 v/v% water was employed in the system.[148] A similar observation was reported, in which CO was photoproduced when CdS was dispersed in DMF under the irradiation of a 500 W mercury lamp with a 300 nm cut off filter.[140] When DMF was substituted with a low polarity solvent, such as CCl_4 and CH_2Cl_2, CO production was dominant, whereas when using a high polar solvent, such as H_2O, formate was produced. This was because the adsorbability of the $CO_2^{\bullet-}$, an intermediate species after the activation of CO_2, was strongly dependent on the polarity of the solvent used. For instance, low polarity molecules enabled strong adsorption of $CO_2^{\bullet-}$ on the Cd sites of CdS through the carbon atom of $CO_2^{\bullet-}$, which was not highly solvated in solvents of low polarity, resulting in the formation of CO. When high polar solvents were used, $CO_2^{\bullet-}$ was stabilised in the system and established only weak interactions with the photocatalyst. As a result, $CO_2^{\bullet-}$ tended to react with a proton and produced formate.

A recent study suggested that the CO_2 photoreduction process can be greener when glycerol, which is a green solvent derived from vegetable oil, was used as the hole scavenger instead of petroleum-derived solvents.[141] In this study, wurtzite ZnS facilitated the photoproduction of formic acid from CO_2 with an apparent quantum efficiency of 3.2% and 0.9% when glycerol and 2-propanol, respectively, were employed as the hole scavenger.

Cyclohexanol was used as the hole scavenger for the CO_2 photoreduction under UV light irradiation.[149] The optimised sample exhibited the production of cyclohexyl formate and cyclohexanone (178.1 and 170.2 μmol $g_{catalyst}^{-1}$, respectively) after 8 h. The authors elucidated that the production of cyclohexanone was slightly lower than that of cyclohexyl formate because some of the photogenerated holes were consumed by cyclohexanol to form cyclohexyl ether.

A recent study demonstrated that a Ru(II)-complex/C_3N_4 nanocomposite could induce the photocatalytic CO_2 reduction by using a mixture of solvents (*N*,*N*-dimethylacetamide and DMA/TEOA).[142] The apparent quantum efficiency achieved was 5.7% at 400 nm (Table 2 Entry 12). In addition, the product selectivity of the Ru(II)-complex/C_3N_4 nanocomposite could be enhanced through manipulating the solvent used (Fig. 13).[145]

In order to avoid using organic solvents as the medium, the mononuclear Ru(II) complex proposed in a previous study[142] was replaced with a binuclear Ru(II) complex coupled with Ag/C_3N_4 and was employed as the photocatalyst (Table 2 entry 13).[143] Since no reduction product was obtained in pure water, a hole scavenger (ethylenediaminetetraacetic acid disodium salt dihydrate, EDTA·Na_2) was added to promote the photocatalytic CO_2 reduction in water. The main product was HCOOH, and H_2 was produced as a by-product under visible light irradiation (λ > 400 nm). Other hole scavenging agents (*e.g.*, potassium oxalate and sodium ascorbate) were shown to be useful for the CO_2PR. Among the three hole scavenging agents, sodium ascorbate exhibited the best performance with 31.7 μmol and 86% selectivity towards HCOOH. The HCOOH production could be further enhanced to 83.3 μmol with selectivity 97% when K_2CO_3 (0.1 M) was used as an additive.[144] However, the production of H_2 was reduced by half.

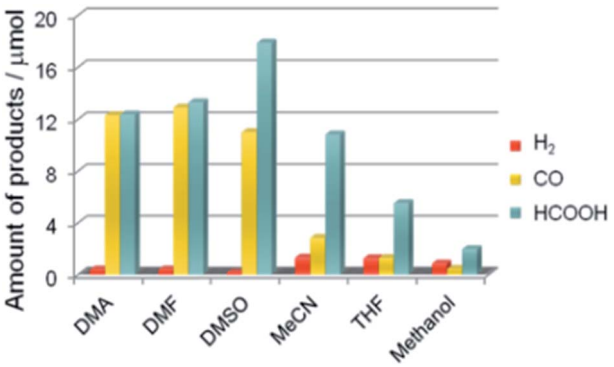

Fig. 13 Product distribution of visible light (λ > 400 nm) CO_2 reduction using Ru(II) complex/C_3N_4 as a photocatalyst and various solvents under a CO_2 atmosphere (DMSO: dimethyl sulfoxide, MeCN: acetonitrile, and THF: tetrahydrofuran). Reproduced from ref. 145 with permission.

The introduction of organic and inorganic hole scavenging agents has exhibited advantages to enhance the efficiency of CO_2PR. The presence of hole scavenging agents in the CO_2PR process is necessary if the oxidation reaction in the CO_2PR cannot be inhibited by the photocatalyst. Moreover, to avoid carbon contamination and false positive errors for the photogeneration of hydrocarbons in the CO_2PR process, inorganic hole scavenging agents are preferred.

4. Conclusions and future directions

To date, significant achievements have been made in the design and fabrication of photocatalysts and the optimisation of photocatalytic systems. CO_2PR using metal sulphides, oxides, oxynitrides and nitrides accumulated so far have offered alternative photocatalytic materials other than TiO_2. Material properties, including the surface area, light harvesting, and charge generation, separation and transportation, have been manipulated through the structural and morphological control during the fabrication processes, leading to enhanced CO_2PR performance. Amongst the non-titania photocatalysts (metal sulphides, oxides, oxynitrides and nitrides) reviewed here, the ultrathin $W_{18}O_{49}$ exhibited the highest CH_4 yield (2200 μmol $g_{catalyst}^{-1}$ h^{-1}) from CO_2 under visible light irradiation. The

presence of oxygen vacancies was suggested to play an important role in the CO_2PR. On the other hand, the addition of inorganic salts or organic solvents into an aqueous system has shown to effectively scavenge the photogenerated holes and/or increase CO_2 solubility.

Although significant studies have been carried out on CO_2PR, some challenges still remain. Firstly, an in-depth understanding of the working mechanism in a CO_2 photoreduction process is still not well understood. Hence, a trial-and-error approach was used when fabricating photocatalysts, attempting to achieve a high CO_2PR efficiency. Secondly, the insight into the CO_2PR in the presence of hole scavenging agent(s) is not available. Moreover, due to this lack of knowledge, a rational design to combine state-of-art of photocatalysts with the desired hole scavenging agent(s) for carbon fuel production is difficult to achieve. Therefore, while more effort is required in material advancement, studies of the combined effect of the proposed photocatalyst with a hole scavenger should be encouraged. In addition, further investigation of CO_2PR at the molecular level through *in situ* characterisation techniques should be carried out as this is key to boosting the efficiency of CO_2PR.

Conflicts of interest

There are no conflicts to declare.

Acknowledgements

The authors acknowledge the financial support provided by the Engineering and Physical Sciences Research Council (EP/K021796/1), the Research Centre for Carbon Solutions (RCCS) and the Robert Buchan Chair in Sustainable Energy Engineering at Heriot-Watt University.

References

1 J. H. Montoya, L. C. Seitz, P. Chakthranont, A. Vojvodic, T. F. Jaramillo and J. K. Nørskov, *Nat. Mater.*, 2016, **16**, 70.
2 IEA Finds CO_2 Emissions Flat for Third Straight Year Even as Global Economy Grew in 2016, https://www.iea.org/newsroom/news/2017/march/iea-finds-co2-emissions-flat-for-third-straight-year-even-as-global-economy-grew.html.
3 Forecast of Worldwide Carbon Dioxide Emissions through 2040, https://www.statista.com/statistics/263980/forecast-of-global-carbon-dioxide-emissions/.
4 T. Inoue, A. Fujishima, S. Konishi and K. Honda, *Nature*, 1979, **277**, 637–638.
5 K. R. Thampi, J. Kiwi and M. Gratzel, *Nature*, 1987, **327**, 506–508.
6 Y. Y. Lee, H. S. Jung and Y. T. Kang, *J. CO2 Util.*, 2017, **20**, 163–177.
7 S. N. Habisreutinger, L. Schmidt-Mende and J. K. Stolarczyk, *Angew. Chem., Int. Ed.*, 2013, **52**, 7372–7408.
8 M. Marszewski, S. Cao, J. Yu and M. Jaroniec, *Mater. Horiz.*, 2015, **2**, 261–278.
9 K. Li, X. An, K. H. Park, M. Khraisheh and J. Tang, *Catal. Today*, 2014, **224**, 3–12.
10 J. L. White, M. F. Baruch, J. E. Pander, Y. Hu, I. C. Fortmeyer, J. E. Park, T. Zhang, K. Liao, J. Gu, Y. Yan, T. W. Shaw, E. Abelev and A. B. Bocarsly, *Chem. Rev.*, 2015, **115**, 12888–12935.
11 Y. Yamazaki, H. Takeda and O. Ishitani, *J. Photochem. Photobiol., C*, 2015, **25**, 106–137.
12 P. Salvador, *J. Appl. Phys.*, 1984, **55**, 2977–2985.
13 O. Carp, C. L. Huisman and A. Reller, *Prog. Solid State Chem.*, 2004, **32**, 33–177.
14 O. Ola and M. M. Maroto-Valer, *J. Photochem. Photobiol., C*, 2015, **24**, 16–42.
15 M. S. Akple, J. Low, Z. Qin, S. Wageh, A. A. Al-Ghamdi, J. Yu and S. Liu, *Chin. J. Catal.*, 2015, **36**, 2127–2134.
16 K. Sasan, F. Zuo, Y. Wang and P. Feng, *Nanoscale*, 2015, **7**, 13369–13372.
17 H. Zhao, L. Liu, J. M. Andino and Y. Li, *J. Mater. Chem. A*, 2013, **1**, 8209–8216.
18 S.-M. Park, A. Razzaq, Y. H. Park, S. Sorcar, Y. Park, C. A. Grimes and S.-I. In, *ACS Omega*, 2016, **1**, 868–875.
19 J. Xiao, D. Mao, X. Guo and J. Yu, *Energy Technol.*, 2015, **3**, 32–39.
20 G. Qin, Y. Zhang, X. Ke, X. Tong, Z. Sun, M. Liang and S. Xue, *Appl. Catal., B*, 2013, **129**, 599–605.
21 E.-G. Ha, J.-A. Chang, S.-M. Byun, C. Pac, D.-M. Jang, J. Park and S. O. Kang, *Chem. Commun.*, 2014, **50**, 4462–4464.
22 Y. Liao, S.-W. Cao, Y. Yuan, Q. Gu, Z. Zhang and C. Xue, *Chem. - Eur. J.*, 2014, **20**, 10220–10222.
23 Q. Zhang, T. Gao, J. M. Andino and Y. Li, *Appl. Catal., B*, 2012, **123–124**, 257–264.
24 J. Low, B. Cheng and J. Yu, *Appl. Surf. Sci.*, 2017, **392**, 658–686.
25 P. Reñones, A. Moya, F. Fresno, L. Collado, J. J. Vilatela and V. A. de la Peña O'Shea, *J. CO2 Util.*, 2016, **15**, 24–31.
26 X. Chang, T. Wang and J. Gong, *Energy Environ. Sci.*, 2016, **9**, 2177–2196.
27 H. Tong, S. Ouyang, Y. Bi, N. Umezawa, M. Oshikiri and J. Ye, *Adv. Mater.*, 2012, **24**, 229–251.
28 Z. Zhu, Y. Han, C. Chen, Z. Ding, J. Long and Y. Hou, *ChemCatChem*, 2018, **10**, 1627–1634.
29 J. Yu, J. Jin, B. Cheng and M. Jaroniec, *J. Mater. Chem. A*, 2014, **2**, 3407–3416.
30 X. Li, J. Wen, J. Low, Y. Fang and J. Yu, *Sci. China Mater.*, 2014, **57**, 70–100.
31 J.-y. Tang, R.-t. Guo, W.-g. Zhou, C.-y. Huang and W.-g. Pan, *Appl. Catal., B*, 2018, **237**, 802–810.
32 P. Xia, B. Zhu, J. Yu, S. Cao and M. Jaroniec, *J. Mater. Chem. A*, 2017, **5**, 3230–3238.
33 W. Yu, D. Xu and T. Peng, *J. Mater. Chem. A*, 2015, **3**, 19936–19947.
34 M. Wang, J. Liu, C. Guo, X. Gao, C. Gong, Y. Wang, B. Liu, X. Li, G. G. Gurzadyan and L. Sun, *J. Mater. Chem. A*, 2018, **6**, 4768–4775.
35 N. Nie, F. He, L. Zhang and B. Cheng, *Appl. Surf. Sci.*, 2018, **457**, 1096–1102.

36 Y. Ma, Z. Wang, X. Xu and J. Wang, *Chin. J. Catal.*, 2017, **38**, 1956–1969.
37 H. Zhao, X. Yang, R. Xu, J. Li, S. Gao and R. Cao, *J. Mater. Chem. A*, 2018, **6**, 20152–20160.
38 Y. Chen, D. Wang, X. Deng and Z. Li, *Catal. Sci. Tech.*, 2017, **7**, 4893–4904.
39 S. Ye, R. Wang, M.-Z. Wu and Y.-P. Yuan, *Appl. Surf. Sci.*, 2015, **358**, 15–27.
40 A. Nikokavoura and C. Trapalis, *Appl. Surf. Sci.*, 2017, **391**, 149–174.
41 X. Chen, S. Shen, L. Guo and S. S. Mao, *Chem. Rev.*, 2010, **110**, 6503–6570.
42 K. Maeda and K. Domen, *J. Phys. Chem. C*, 2007, **111**, 7851–7861.
43 K. Maeda and K. Domen, *J. Phys. Chem. Lett.*, 2010, **1**, 2655–2661.
44 G. Liu, P. Niu, C. Sun, S. C. Smith, Z. Chen, G. Q. Lu and H.-M. Cheng, *J. Am. Chem. Soc.*, 2010, **132**, 11642–11648.
45 W.-N. Wang, W.-J. An, B. Ramalingam, S. Mukherjee, D. M. Niedzwiedzki, S. Gangopadhyay and P. Biswas, *J. Am. Chem. Soc.*, 2012, **134**, 11276–11281.
46 Y. Wei, J. Jiao, Z. Zhao, W. Zhong, J. Li, J. Liu, G. Jiang and A. Duan, *J. Mater. Chem. A*, 2015, **3**, 11074–11085.
47 Z. Hu, M. Xu, Z. Shen and J. C. Yu, *J. Mater. Chem. A*, 2015, **3**, 14046–14053.
48 F. R. F. Fan, P. Leempoel and A. J. Bard, *J. Electrochem. Soc.*, 1983, **130**, 1866–1875.
49 K. Kočí, L. Matějová, O. Kozák, L. Čapek, V. Valeš, M. Reli, P. Praus, K. Šafářová, A. Kotarba and L. Obalová, *Appl. Catal., B*, 2014, **158–159**, 410–417.
50 P. Johne and H. Kisch, *J. Photochem. Photobiol., A*, 1997, **111**, 223–228.
51 D. Meissner, R. Memming and B. Kastening, *J. Phys. Chem.*, 1988, **92**, 3476–3483.
52 X. Meng, G. Zuo, P. Zong, H. Pang, J. Ren, X. Zeng, S. Liu, Y. Shen, W. Zhou and J. Ye, *Appl. Catal., B*, 2018, **237**, 68–73.
53 C. Yang, Q. Li, Y. Xia, K. Lv and M. Li, *Appl. Surf. Sci.*, 2019, **464**, 388–395.
54 Y. Chai, J. Lu, L. Li, D. Li, M. Li and J. Liang, *Catal. Sci. Tech.*, 2018, **8**, 2697–2706.
55 Z. Zhu, J. Qin, M. Jiang, Z. Ding and Y. Hou, *Appl. Surf. Sci.*, 2017, **391**, 572–579.
56 H. Kisch and P. Lutz, *Photochem. Photobiol. Sci.*, 2002, **1**, 240–245.
57 K. Kočí, P. Praus, M. Edelmannová, A. Nela, N. ová, I. Troppová, D. Fridrichová, G. owik and J. Ryczkowski, *J. Nanosci. Nanotechnol.*, 2017, **17**, 4041–4047.
58 P. Li, X. Zhang, C. Hou, L. Lin, Y. Chen and T. He, *Phys. Chem. Chem. Phys.*, 2018, **20**, 16985–16991.
59 X. Li, J. Chen, H. Li, J. Li, Y. Xu, Y. Liu and J. Zhou, *J. Nat. Gas Chem.*, 2011, **20**, 413–417.
60 P. Kar, S. Farsinezhad, X. Zhang and K. Shankar, *Nanoscale*, 2014, **6**, 14305–14318.
61 J. Jin and T. He, *Appl. Surf. Sci.*, 2017, **394**, 364–370.
62 J. Jin, J. Yu, D. Guo, C. Cui and W. Ho, *Small*, 2015, **11**, 5262–5271.
63 W. Li, D. Li, W. Zhang, Y. Hu, Y. He and X. Fu, *J. Phys. Chem. C*, 2010, **114**, 2154–2159.
64 Q. Li, H. Meng, P. Zhou, Y. Zheng, J. Wang, J. Yu and J. Gong, *ACS Catal.*, 2013, **3**, 882–889.
65 Z. Han, G. Chen, C. Li, Y. Yu and Y. Zhou, *J. Mater. Chem. A*, 2015, **3**, 1696–1702.
66 Y. Zhao, H. Pan, Y. Lou, X. Qiu, J. Zhu and C. Burda, *J. Am. Chem. Soc.*, 2009, **131**, 4253–4261.
67 W. Liang and M. H. Whangbo, *Solid State Commun.*, 1993, **85**, 405–408.
68 T. Arai, S. Tajima, S. Sato, K. Uemura, T. Morikawa and T. Kajino, *Chem. Commun.*, 2011, **47**, 12664–12666.
69 J.-Y. Liu, B. Garg and Y.-C. Ling, *Green Chem.*, 2011, **13**, 2029–2031.
70 A. Bachmeier, S. Hall, S. W. Ragsdale and F. A. Armstrong, *J. Am. Chem. Soc.*, 2014, **136**, 13518–13521.
71 A. Kubacka, M. Fernández-García and G. Colón, *Chem. Rev.*, 2012, **112**, 1555–1614.
72 H. W. Eng, P. W. Barnes, B. M. Auer and P. M. Woodward, *J. Solid State Chem.*, 2003, **175**, 94–109.
73 Z. Sheng, K. Piyush, T. Ujwal Kumar and S. Karthik, *Nanotechnology*, 2018, **29**, 052001.
74 A. H. Yahaya, M. A. Gondal and A. Hameed, *Chem. Phys. Lett.*, 2004, **400**, 206–212.
75 J. Núñez, V. A. de la Peña O'Shea, P. Jana, J. M. Coronado and D. P. Serrano, *Catal. Today*, 2013, **209**, 21–27.
76 L. Wan, X. Wang, S. Yan, H. Yu, Z. Li and Z. Zou, *CrystEngComm*, 2012, **14**, 154–159.
77 Q. Liu, Y. Zhou, J. Kou, X. Chen, Z. Tian, J. Gao, S. Yan and Z. Zou, *J. Am. Chem. Soc.*, 2010, **132**, 14385–14387.
78 S. Yan, L. Wan, Z. Li and Z. Zou, *Chem. Commun.*, 2011, **47**, 5632–5634.
79 Q. Liu, Y. Zhou, Z. Tian, X. Chen, J. Gao and Z. Zou, *J. Mater. Chem.*, 2012, **22**, 2033–2038.
80 Q. Liu, D. Wu, Y. Zhou, H. Su, R. Wang, C. Zhang, S. Yan, M. Xiao and Z. Zou, *ACS Appl. Mater. Interfaces*, 2014, **6**, 2356–2361.
81 Z. Li, Y. Zhou, J. Zhang, W. Tu, Q. Liu, T. Yu and Z. Zou, *Cryst. Growth Des.*, 2012, **12**, 1476–1481.
82 J. Guo, K. Wang and X. Wang, *Catal. Sci. Tech.*, 2017, **7**, 6013–6025.
83 Y. P. Xie, G. Liu, L. Yin and H.-M. Cheng, *J. Mater. Chem.*, 2012, **22**, 6746–6751.
84 X. Chen, Y. Zhou, Q. Liu, Z. Li, J. Liu and Z. Zou, *ACS Appl. Mater. Interfaces*, 2012, **4**, 3372–3377.
85 G. Xi, S. Ouyang, P. Li, J. Ye, Q. Ma, N. Su, H. Bai and C. Wang, *Angew. Chem., Int. Ed.*, 2012, **51**, 2395–2399.
86 Y. Zhou, Z. Tian, Z. Zhao, Q. Liu, J. Kou, X. Chen, J. Gao, S. Yan and Z. Zou, *ACS Appl. Mater. Interfaces*, 2011, **3**, 3594–3601.
87 H. Cheng, B. Huang, Y. Liu, Z. Wang, X. Qin, X. Zhang and Y. Dai, *Chem. Commun.*, 2012, **48**, 9729–9731.
88 H. Shi, T. Wang, J. Chen, C. Zhu, J. Ye and Z. Zou, *Catal. Lett.*, 2011, **141**, 525–530.
89 X. Li, H. Pan, W. Li and Z. Zhuang, *Appl. Catal., A*, 2012, **413–414**, 103–108.

90 R. Pang, K. Teramura, H. Asakura, S. Hosokawa and T. Tanaka, *Appl. Catal., B*, 2017, **218**, 770–778.
91 X.-J. Lv, W.-F. Fu, C.-Y. Hu, Y. Chen and W.-B. Zhou, *RSC Adv.*, 2013, **3**, 1753–1757.
92 C.-W. Tsai, H. M. Chen, R.-S. Liu, K. Asakura and T.-S. Chan, *J. Phys. Chem. C*, 2011, **115**, 10180–10186.
93 T. Takayama, H. Nakanishi, M. Matsui, A. Iwase and A. Kudo, *J. Photochem. Photobiol., A*, 2017, **358**, 416–421.
94 H. Nakanishi, K. Iizuka, T. Takayama, A. Iwase and A. Kudo, *ChemSusChem*, 2017, **10**, 112–118.
95 Z. Huang, K. Teramura, H. Asakura, S. Hosokawa and T. Tanaka, *Catal. Today*, 2018, **300**, 173–182.
96 M. Yamamoto, T. Yoshida, N. Yamamoto, H. Yoshida and S. Yagi, *e-J. Surf. Sci. Nanotechnol.*, 2014, **12**, 299–303.
97 J. Mao, T. Peng, X. Zhang, K. Li and L. Zan, *Catal. Commun.*, 2012, **28**, 38–41.
98 J. W. Lekse, M. K. Underwood, J. P. Lewis and C. Matranga, *J. Phys. Chem. C*, 2012, **116**, 1865–1872.
99 K. Wang, L. Zhang, Y. Su, D. Shao, S. Zeng and W. Wang, *J. Mater. Chem. A*, 2018, **6**, 8366–8373.
100 Q. Han, Y. Zhou, L. Tang, P. Li, W. Tu, L. Li, H. Li and Z. Zou, *RSC Adv.*, 2016, **6**, 90792–90796.
101 S. Yan, H. Yu, N. Wang, Z. Li and Z. Zou, *Chem. Commun.*, 2012, **48**, 1048–1050.
102 B. AlOtaibi, S. Fan, D. Wang, J. Ye and Z. Mi, *ACS Catal.*, 2015, **5**, 5342–5348.
103 T.-M. Su, Z.-z. Qin, H.-B. Ji, Y.-x. Jiang and G. Huang, *Environ. Chem. Lett.*, 2016, **14**, 99–112.
104 G. Mahmodi, S. Sharifnia, F. Rahimpour and S. N. Hosseini, *Sol. Energy Mater. Sol. Cells*, 2013, **111**, 31–40.
105 J. Xiao, W. Yang, S. Gao, C. Sun and Q. Li, *J. Mater. Sci. Technol.*, 2018, **34**, 2331–2336.
106 G. R. Bamwenda and H. Arakawa, *Appl. Catal., A*, 2001, **210**, 181–191.
107 S. Xie, Y. Wang, Q. Zhang, W. Deng and Y. Wang, *Chem. Commun.*, 2015, **51**, 3430–3433.
108 W.-J. Chun, A. Ishikawa, H. Fujisawa, T. Takata, J. N. Kondo, M. Hara, M. Kawai, Y. Matsumoto and K. Domen, *J. Phys. Chem. B*, 2003, **107**, 1798–1803.
109 S. Sato, T. Morikawa, S. Saeki, T. Kajino and T. Motohiro, *Angew. Chem., Int. Ed.*, 2010, **49**, 5101–5105.
110 P.-W. Pan and Y.-W. Chen, *Catal. Commun.*, 2007, **8**, 1546–1549.
111 H.-C. Chen, H.-C. Chou, J. C. S. Wu and H.-Y. Lin, *J. Mater. Res.*, 2011, **23**, 1364–1370.
112 K. Li, A. D. M. Handoko, M. Khraisheh and J. Tang, *Nanoscale*, 2014, **6**, 9767–9773.
113 Z. Huang, K. Teramura, S. Hosokawa and T. Tanaka, *Appl. Catal., B*, 2016, **199**, 272–281.
114 L. Chen, D. Meng, X. Wu, A. Wang, J. Wang, Y. Wang and M. Yu, *J. Phys. Chem. C*, 2016, **120**, 18548–18559.
115 X.-J. Wen, C.-G. Niu, L. Zhang, C. Liang and G.-M. Zeng, *Appl. Catal., B*, 2018, **221**, 701–714.
116 W. Xiong, W. Dai, X. Hu, L. Yang, T. Wang, Y. Qin, X. Luo and J. Zou, *Mater. Lett.*, 2018, **232**, 36–39.
117 Q. Zhang, M. Mao, Y. Li, Y. Yang, H. Huang, Z. Jiang, Q. Hu, S. Wu and X. Zhao, *Appl. Catal., B*, 2018, **239**, 555–564.
118 Y. Kohno, H. Ishikawa, T. Tanaka, T. Funabiki and S. Yoshida, *Phys. Chem. Chem. Phys.*, 2001, **3**, 1108–1113.
119 H.-a. Park, J. H. Choi, K. M. Choi, D. K. Lee and J. K. Kang, *J. Mater. Chem.*, 2012, **22**, 5304–5307.
120 Y. Tong, Y. Zhang, N. Tong, Z. Zhang, Y. Wang, X. Zhang, S. Zhu, F. Li and X. Wang, *Catal. Sci. Tech.*, 2016, **6**, 7579–7585.
121 K. Wang, L. Zhang, Y. Su, S. Sun, Q. Wang, H. Wang and W. Wang, *Catal. Sci. Tech.*, 2018, **8**, 3115–3122.
122 Y. Chen, G. Jia, Y. Hu, G. Fan, Y. H. Tsang, Z. Li and Z. Zou, *Sustainable Energy Fuels*, 2017, **1**, 1875–1898.
123 D. E. Scaife, *Sol. Energy*, 1980, **25**, 41–54.
124 K. Maeda, *Prog. Solid State Chem.*, 2018, **51**, 52–62.
125 K. Maeda, *Phys. Chem. Chem. Phys.*, 2013, **15**, 10537–10548.
126 M. Hara, G. Hitoki, T. Takata, J. N. Kondo, H. Kobayashi and K. Domen, *Catal. Today*, 2003, **78**, 555–560.
127 Q. Gao, C. Giordano and M. Antonietti, *Small*, 2011, **7**, 3334–3340.
128 F. Yoshitomi, K. Sekizawa, K. Maeda and O. Ishitani, *ACS Appl. Mater. Interfaces*, 2015, **7**, 13092–13097.
129 K. Muraoka, H. Kumagai, M. Eguchi, O. Ishitani and K. Maeda, *Chem. Commun.*, 2016, **52**, 7886–7889.
130 N. Zhang, S. Ouyang, T. Kako and J. Ye, *Chem. Commun.*, 2012, **48**, 1269–1271.
131 H. L. Tuller, *Mater. Renewable Sustainable Energy*, 2017, **6**, 3.
132 M. Kanemoto, T. Shiragami, C. Pac and S. Yanagida, *J. Phys. Chem.*, 1992, **96**, 3521–3526.
133 R. Zhou and M. I. Guzman, *J. Phys. Chem. C*, 2014, **118**, 11649–11656.
134 X. Meng, Q. Yu, G. Liu, L. Shi, G. Zhao, H. Liu, P. Li, K. Chang, T. Kako and J. Ye, *Nano Energy*, 2017, **34**, 524–532.
135 S. Kaneco, Y. Shimizu, K. Ohta and T. Mizuno, *J. Photochem. Photobiol., A*, 1998, **115**, 223–226.
136 I. H. Tseng, W.-C. Chang and J. C. S. Wu, *Appl. Catal., B*, 2002, **37**, 37–48.
137 S. Liu, Z. Zhao and Z. Wang, *Photochem. Photobiol. Sci.*, 2007, **6**, 695–700.
138 K. Teramura, Z. Wang, S. Hosokawa, Y. Sakata and T. Tanaka, *Chem. Eur. J.*, 2014, **20**, 9906–9909.
139 S. Iguchi, K. Teramura, S. Hosokawa and T. Tanaka, *Phys. Chem. Chem. Phys.*, 2015, **17**, 17995–18003.
140 B.-J. Liu, T. Torimoto and H. Yoneyama, *J. Photochem. Photobiol., A*, 1998, **113**, 93–97.
141 D. P. Leonard, H. Pan and M. D. Heagy, *ACS Appl. Mater. Interfaces*, 2016, **8**, 1553.
142 R. Kuriki, K. Sekizawa, O. Ishitani and K. Maeda, *Angew. Chem., Int. Ed.*, 2015, **54**, 2406–2409.
143 R. Kuriki, H. Matsunaga, T. Nakashima, K. Wada, A. Yamakata, O. Ishitani and K. Maeda, *J. Am. Chem. Soc.*, 2016, **138**, 5159–5170.

144 R. Kuriki, M. Yamamoto, K. Higuchi, Y. Yamamoto, M. Akatsuka, D. Lu, S. Yagi, T. Yoshida, O. Ishitani and K. Maeda, *Angew. Chem., Int. Ed.*, 2017, **56**, 4867–4871.
145 R. Kuriki, O. Ishitani and K. Maeda, *ACS Appl. Mater. Interfaces*, 2016, **8**, 6011–6018.
146 I. Hiroshi, T. Tsukasa, S. Takao, M. Hirotaro and Y. Hiroshi, *Chem. Lett.*, 1990, **19**, 1483–1486.
147 H. Inoue, H. Moriwaki, K. Maeda and H. Yoneyama, *J. Photochem. Photobiol., A*, 1995, **86**, 191–196.
148 K. Masashi, I. Ken-ichi, W. Yuji, S. Takao, M. Hirotaro and Y. Shozo, *Chem. Lett.*, 1992, **21**, 835–836.
149 G. Song, F. Xin and X. Yin, *J. Colloid Interface Sci.*, 2015, **442**, 60–66.